TFAP2 paralogs pioneer chromatin access for MITF and directly inhibit genes associated with cell migration

Colin Kenny[1], Ramile Dilshat [2], Hannah Seberg[1+], Eric Van Otterloo[1*], Gregory Bonde[1], Annika Helverson[1], Eiríkur Steingrímsson[2], Robert A. Cornell[1, #]

1. Department of Anatomy and Cell Biology, College of Medicine, University of Iowa, Iowa City, Iowa

2. Department of Biochemistry and Molecular Biology, BioMedical Center, Faculty of Medicine, University of Iceland, Sturlugata 8, 101 Reykjavik, Iceland

[+] Current address: University of Manchester

* Current address: Iowa Institute for Oral Health Research, Department of Anatomy and Cell Biology, Department of Periodontics, College of Dentistry, University of Iowa, Iowa City, Iowa

[#]Corresponding author:

Robert-cornell@uiowa.edu, 319-335-8908

Conflict of interest statement: CK, RD, HS, EVO, GB, AH, ES and RAC declare no conflicts of interest.

Key words: MITF, TFAP2A, TFAP2C, chromatin, nucleosome, pioneer factor, transcriptional activation, repression.

Abstract

Transcription factors in the Activating-enhancer-binding Protein 2 (TFAP2) family redundantly regulate gene expression in melanocytes and melanoma. Previous ChIP-seq experiments indicate that TFAP2A and Microphthalmia-associated Transcription Factor (MITF), a master regulator in these cell types, co-activate enhancers of genes promoting pigmentation. Evidence that TFAP2 paralogs can serve as pioneer factors supports the possibility that TFAP2 facilitates MITF binding at co-bound enhancers, although this model has not been tested. In addition, while MITF and TFAP2 paralogs both appear to repress genes that promote invasion, whether they do so by co-repressing enhancers is unknown. To address these questions we evaluated gene expression, chromatin accessibility, TFAP2A and MITF binding, and chromatin marks characteristic of active enhancers in SK-MEL-28 melanoma cells that were wild-type or deleted of the two *TFAP2* paralogs with highest expression, *TFAP2A* and *TFAP2C* (i.e., *TFAP2*-KO cells). Integrated analyses revealed distinct subsets of enhancers bound by TFAP2A in WT cells that are inactivated and activated, respectively, in *TFAP2*-KO cells. At enhancers bound by both MITF and TFAP2A, MITF is generally lost in *TFAP2A/TFAP2C* double mutants, but not vice versa, implying TFAP2 pioneers chromatin access for MITF. There is a strong correlation between the sets of genes inhibited by MITF and TFAP2, although we did not find evidence that TFAP2 and MITF inhibit enhancers cooperatively. The findings imply that MITF and TFAP2 paralogs cooperatively affect the melanoma phenotype.

Introduction

Gene expression in developing melanocytes and melanoma, a cancer derived from the melanocyte lineage, is regulated by transcription factors including Microphthalmia-associated transcription factor (MITF) and members of the SOXE, PAX and TFAP2 families (Atchison, 2014; Betancur et al., 2010; Eckert et al., 2005; Goding, 2000; Hartman and Czyz, 2015; Hoek et al., 2008b; Mollaaghababa and Pavan, 2003; Seberg et al., 2017a; Strub et al., 2011; Van Otterloo et al., 2010; Van Otterloo et al., 2012). MITF is required for differentiation of melanocytes during development, and its activity is regulated at both the transcriptional and post-

translational levels (Rambow et al., 2019). In melanoma cells, high levels of MITF activity promote cell proliferation and pigmentation, while lower levels promote an invasive phenotype (Carreira et al., 2006; Rambow et al., 2019). Mass spectroscopy revealed that MITF interacts with components of both the PBAF chromatin remodeling complex, including BRG1 and CDH7, and the NURF remodeling complex, including RBBP4 (de la Serna et al., 2006; Laurette et al., 2015). Furthermore, chromatin immunoprecipitation of BRG1 in cells depleted of *MITF* revealed that MITF recruits BRG1 to the promoters of specific genes, including *TYR*, which encodes the rate-limiting enzyme in melanin synthesis Tyrosinase (Laurette et al., 2015). Similar analysis suggested that SOX10 also recruits BRG1 to chromatin, and at some loci it does so in co-operation with MITF (Laurette et al., 2015). Conversely, there is evidence that PAX3 inhibits the activity of MITF at the *DCT* promoter (Lang et al., 2005). Furthermore, low MITF activity is associated with an invasive phenotype, and deletion or knockdown of *MITF* results in upregulation of genes that promote migration and invasion (Dilshat et al., 2021). MITF CUT&RUN peaks are found near some genes whose expression is upregulated in *MITF* mutant cells, implying MITF directly represses their expression (Dilshat et al., 2021).This set of MITF peaks is enriched for the binding site of FOXC1, a transcriptional repressor (Du et al., 2012), suggesting MITF has co-factors in its repressive function as well as its activating one.

The activating enhancer-binding family of transcription factors, comprising five members, TFAP2A-E, regulate development of many cell types and organs including neural crest, placodes, epidermis, trophectoderm, heart, kidney, and brain (Bamforth et al., 2001; Brewer et al., 2002; Knight et al., 2003; Kuckenberg et al., 2012; Luo et al., 2002; Mitchell et al., 1991; Moser et al., 1997; Schorle et al., 1996; Tan et al., 2008; Wang et al., 2006). In several contexts, including melanocyte differentiation, TFAP2 paralogs function redundantly (Kołat et al., 2021; Li and Cornell, 2007; Van Otterloo et al., 2010; Wang et al., 2008). For instance, in zebrafish *tfap2a* loss-of-function mutant embryos the number of melanocytes is lower than normal and pigmentation is profoundly delayed relative to in wild type embryos; this phenotype is exacerbated if *tfap2a* mutant embryos are also depleted of *tfap2e* expression with antisense morpholinos (Van Otterloo et al., 2010). In zebrafish melanoma Tfap2a and Tfap2e also appear to act redundantly to promote proliferation and, interestingly,

88 to suppress cell adhesion and cell migration (Campbell et al., 2021). Consistent with
89 redundant function of Tfap2 paralogs in the melanocyte lineage, in the skin of mouse
90 embryos with neural-crest specific knockout of the two paralogs with highest
91 expression, *Tfap2a* and *Tfap2b*, there are fewer-than-normal cells expressing
92 markers of melanocytes (Seberg et al., 2017b).
93
94 Tfap2 paralogs and MITF appear to co-activate certain genes. For instance, in a
95 human melanoma cell line, the *in vitro* enhancer activity of an element within an *IRF4*
96 intron depended on the simultaneous binding of MITF and TFAP2 (Praetorius et al.,
97 2013). Further, in zebrafish *tfap2a* and *mitfa* double mutant embryos there is a
98 greater-than-additive reduction in the number, and level of pigmentation, of
99 melanocytes in comparison to in single mutants (Seberg et al., 2017b). Evidence that
100 Tfap2 paralogs and Mitfa operated in parallel, rather than Tfap2 paralogs functioning
101 upstream of *mitfa* expression, is that in *tfap2a/tfap2e* doubly-depleted zebrafish
102 embryos, *mitfa* expression, and the number of *mitfa*-expressing cells, are not
103 significantly changed from *tfap2a* singly depleted embryos (Seberg et al., 2017b).
104 Supporting parallel activity of Tfap2 paralogs and MITF, the promoters of MITF target
105 genes are enriched for TFAP2 consensus binding sites (Laurette et al., 2015;
106 Rambow et al., 2015). Moreover, ChIP-seq experiments in primary melanocytes
107 suggest that TFAP2A and MITF bind overlapping regions of chromatin near genes
108 encoding regulators of pigmentation (Seberg et al., 2017b). Collectively, these
109 observations indicate that TFAP2 paralogs co-activate a subset of MITF target genes
110 by binding at the same enhancers. Still unclear, however, is whether they also co-
111 repress enhancers, and whether TFAP2 paralogs and MITF act cooperatively or
112 independently at enhancers they co-regulate.

113 TFAP2 paralogs may serve as pioneer factors for MITF, although not all evidence
114 supports this possibility. *Pioneer* or *initiating* TFs can bind nucleosome-bound DNA
115 and recruit other TFs that lack this property called *settler TFs* (reviewed in Voss and
116 Hager, 2014; Zaret, 2020; Zaret and Carroll, 2011). Evidence that TFAP2 paralogs
117 are pioneer factors includes, first, that TFAP2 binding site is over-represented within
118 DNase1-protected “footprints” in mouse embryonic stem cells induced to differentiate
119 (Sherwood et al., 2014). Second, TFAP2A catalyzes assisted loading of androgen
120 receptor (AR) in epididymis cells (Pihlajamaa et al., 2014) and estrogen receptor in

121 MCF-7 cells (Tan et al., 2011). Third, the TFAP2 binding site is enriched for at the
122 center of ATAC-seq peaks, implying it has a strong effect on chromatin accessibility
123 (Grossman et al., 2018). Fourth, ATAC-seq peaks in naïve-stated human ESC
124 showed reduced openness in TFAP2C KO cells (Pastor et al., 2018), and forcing
125 expression of TFAP2C in human ESC is sufficient to open chromatin at loci where it
126 binds (Li et al., 2019). Finally, TFAP2A, TFAP2B and TFAP2C can bind
127 nucleosomes (Fernandez Garcia et al., 2019). Together these findings support the
128 possibility that TFAP2 displaces nucleosomes and thereby facilitates chromatin
129 binding by MITF. However, it not clear that MITF needs a pioneer factor to bind
130 chromatin. In the *dynamic-assisted-loading model*, all classes of TFs have short
131 residency on chromatin (reviewed in Voss and Hager, 2014). *Initiating TFs* are able
132 to recruit ATP-dependent chromatin remodelers (nBAF, SWI/SNF, INO80, ISWI,
133 NURD) and thereby make chromatin accessible to other TFs, i.e., the *assisted* TFs
134 (Swinstead et al., 2016b). As mentioned above, MITF binds various components of
135 the SWI/SNF complex (Aras et al., 2019; de la Serna et al., 2006; Keenen et al.,
136 2010) and the chromatin remodeler CHD7 (Laurette et al., 2015) and so meets the
137 criteria for an initiating factor. If the dynamic-assisted-loading model holds in this
138 situation, MITF would have no need for a pioneer factor like TFAP2 to assist its
139 binding to chromatin.

140 To address these questions, we systematically tested the effect of loss of TFAP2
141 paralogs on: nucleosome positioning, using the assay for transposase-accessible
142 chromatin using sequencing (ATAC-seq) methodology; enhancer activity, using
143 cleavage under targets and release using nuclease (CUT&RUN) with anti-H3K27Ac,
144 anti-H3K4me3, and anti-H3K27me3; and binding of MITF, using CUT&RUN. We
145 similarly assessed binding of TFAP2A in cells harboring loss of function mutations in
146 *MITF*. Our results support the notion that TFAP2 factors behave like the canonical
147 pioneer factor FOXA1: at many chromatin elements bound by TFAP2A, loss TFAP2
148 led to loss of enhancer activity, and in a large subset, it also let to chromatin
149 becoming condensed. In both of these subsets of TFAP2-activated enhancers, MITF
150 binding was TFAP2 dependent. In addition, we find evidence that TFAP2 paralogs
151 can also inhibit enhancers, and at a subset of those that they inhibit, they exclude
152 binding of MITF. Finally, the analyses suggest TFAP2 directly inhibits many of the
153 same genes that MITF inhibits, but we do not find evidence that TFAP2 and MITF

154 co-repress the same enhancers. Together these findings illuminate the mechanisms
155 by which TFAP2 and MITF coordinately regulate differentiation of melanocytes and
156 the phenotype of melanoma cells.

157 **Results**

158 **Tfap2a and Tfap2e redundantly promote the differentiation of zebrafish**
159 **embryonic melanocytes**

160 We first sought to use a zebrafish mutant to confirm an earlier conclusion based on
161 morpholino-mediated knockdown that Tfap2 paralogs redundantly promote
162 differentiation of embryonic melanophores. In the melanocyte lineage of zebrafish
163 embryos, levels of *tfap2e* expression are high, those of *tfap2a* and *tfap2c* are lower
164 (~30% of the level of *tfap2e*), and those of *tfap2b* are negligible (Higdon et al., 2013).
165 We previously reported that wild-type (WT) embryos injected with antisense
166 morpholino oligonucleotides (MO) targeting the splicing of *tfap2e* exhibit no overt
167 phenotype, but embryos homozygous for a *tfap2a* loss-of-function allele (i.e., lockjaw
168 , Knight et al., 2003), injected with the *tfap2e* MO have fewer embryonic melanocytes
169 than counterparts injected with a non-targeting control MO, and pigmentation is
170 delayed in them, although it occurs eventually (Van Otterloo et al., 2010). To confirm
171 that the recovery of pigmentation did not simply reflect the transient effects of the
172 *tfap2e* morpholino we used zinc-finger nucleases to engineer zebrafish lines
173 harboring frame-shift-inducing mutations in *tfap2e* (details in **Supplemental Fig.**
174 **S1A-B)**. qPCR analysis showed that expression of the *tfap2e* transcript was
175 significantly lower in *tfap2e* mutant than in WT embryos, suggesting nonsense-
176 mediated decay (**Supplemental Fig. S1C**)**.** As in embryos injected with *tfap2e* MO,
177 there was no overt phenotype in homozygous *tfap2e* mutants (**Supplemental Fig.**
178 **S1D-F**). However, in *tfap2a*/*tfap2e* double mutants the number of melanocytes was
179 significantly reduced in the dorsal stripe at 29 hours post fertilization (hpf) relative to
180 those in *tfap2a* single mutants. At this stage these cells were under-pigmented
181 relative to in non-mutant siblings, although their pigmentation reached wild-type
182 levels by 48 hpf (**Fig. 1A-E; Supplemental Fig. S1G-J**). In summary, the reduction
183 in melanocyte number and delay in pigmentation in *tfap2a/tfap2e* double mutant
184 versus WT embryos implies that TFAP2 paralogs promote melanocyte proliferation
185 and differentiation in a redundant fashion.

186 **TFAP2A binds open and closed chromatin**

187 We next sought to learn TFAP2 paralogs interact with MITF in activating and
188 repressing gene expression in a single cell line. We have reported the genes
189 differentially expressed between SK-MEL-28 melanoma cells that are WT or
190 harboring loss-of-function mutations in all alleles of MITF, as well as binding of MITF
191 using cleavage under targets and release under nuclease (CUT&RUN) (Dilshat et
192 al., 2021). Here, again using SK-MEL-28 melanoma cells, we carried out (1)
193 CUT&RUN using antibodies to TFAP2A (i.e., TFAP2A peaks), (2) CUT&RUN using
194 antibodies to chromatin marks indicative of active regulatory elements (H3K27Ac
195 and H3K4Me3) (Creyghton et al., 2010; Pekowska et al., 2011), and of inactive
196 chromatin (H3K27Me3) (Ringrose and Paro, 2004), and (3) ATAC-seq to distinguish
197 between open and closed chromatin (Buenrostro et al., 2013). We used IgG as a
198 background control and the MACS2 software to call peaks in each dataset
199 (**Supplemental Fig. S2A-B**). Based on proximity to transcriptional start sites (TSS),
200 about one-third of TFAP2A peaks appeared to be at or near promoters (within 3 kb
201 of a TSS). As expected, these elements had strong H3K4Me3 signal (**Supplemental**
202 **Fig. S2B**). At promoter-proximal TFAP2A peaks, the H3K27Ac signal in WT cells
203 was relatively consistent, whereas at promoter-distal TFAP2A peaks the H3K27Ac
204 signal ranged from high to background level (**Supplemental Fig. S2B-C**). About two-
205 thirds of TFAP2A peaks overlapped ATAC-seq peaks, indicating that they were in
206 open chromatin (**Supplemental Fig. S2D-E**). Of note, the read depth (height) of a
207 peak approximates the number of chromosome molecules where TFAP2A binds.
208 The average read depth of the TFAP2A peaks in closed chromatin was only about
209 50% of that in open chromatin but was nonetheless 80-fold higher than the IgG
210 background read depth (**Supplemental Fig. S2D-E, Supplemental Fig. S3A-B for**
211 **example loci**). Importantly, the TFAP2 binding site was strongly enriched for in both
212 TFAP2A-bound elements where the local ATAC-seq signal was called as a peak and
213 in counterparts where it was not ($p < 1 \times 10^{-1785}$ and $p < 1 \times 10^{-4375}$, respectively),
214 supporting the idea that TFAP2A binds DNA directly even when the DNA is occupied
215 by nucleosomes (**Supplemental Fig. S3C-D**). These results indicate that TFAP2A
216 binds at both open and closed chromatin, consistent with it being a pioneer factor,
217 and at enhancers and promoters with a range of activity levels.

218

219 **TFAP2A activates enhancers as in pioneer factor and non-pioneer factor**
220 **modes**

221 We next sought to identify enhancers and promoters that TFAP2 paralogs regulate
222 directly, and, of these, the fraction that they regulate as pioneer factors. To these
223 ends we used Crispr/Cas9 methods to introduce frame-shift mutations into the
224 *TFAP2* genes with high expression in SK-MEL-28 cells, *TFAP2A* and *TFAP2C;* we
225 then carried out RNA-seq, ATAC-seq, and CUT&RUN with antibodies to H3K27Ac,
226 H3K4me3, and H3K27me3. In two independent knockout clones (hereafter, *TFAP2*-
227 KO cells), Western blot analysis showed an absence of immunoreactivity for both
228 proteins (**Supplemental Fig. S4A-E**). Control clones (hereafter WT cells) were
229 derived from the parental SK-MEL-28 line transiently transfected with Cas9 but not
230 with guide RNAs. RNA-seq revealed that expression of 532 genes was
231 downregulated, and expression of 609 genes was upregulated, in *TFAP2*-KO cells
232 (i.e., in both clones) versus in WT cells (**Supplemental Fig. S5A volcano plot**). We
233 will refer to these sets as "TFAP2-activated genes" and "TFAP2-inhibited genes,"
234 respectively.

235 To identify candidates for enhancers directly activated by TFAP2 paralogs we first
236 filtered TFAP2A peaks for those in chromatin that was open and active in WT cells
237 (i.e., coinciding with peaks of ATAC-seq and H3K27Ac) (21,745/ 36,948 of TFAP2A
238 peaks), then for those greater than 1 kb from a transcription start site (i.e., to filter out
239 promoters) (11,005/ 21,745), and finally for those where the local H3K27Ac signal
240 was significantly lower (adj $p < 0.05$, log2FC <-1) in *TFAP2*-KO cells relative to in
241 WT cells (3,858/11,005).

242 To determine how often TFAP2 activates enhancers as a pioneer factor, at each
243 directly TFAP2-activated enhancer we evaluated the ATAC-seq signal in WT and
244 TFAP2-KO cells. At about half of the enhancers the ATAC-seq signal was also
245 significantly lower (adj $p < 0.05$, log2FC <-1) in *TFAP2*-KO versus in WT cells (i.e.,
246 the ATAC-seq signal was TFAP2-activated) (**Fig. 2A, E-E'**); at this subset we infer
247 that TFAP2 paralogs function as pioneer factors. At the remaining half, the ATAC-
248 seq signal was unchanged between *TFAP2*-KO versus WT cells (i.e., the ATAC-seq

signal was TFAP2-independent) (**Fig. 2B, F-F'**); at this subset we infer that TFAP2 paralogs do not function as pioneer factors but rather as a transcriptional activator. Consistent with both subsets indeed being enhancers activated by TFAP2, both were associated with TFAP2-activated genes. Interestingly, the association was stronger for those where TFAP2 functions as a pioneer factor (**Fig. 2 I, J**) (**Table 1 and Table 2**). Moreover, at both subsets the H3K4me3 signal, which is associated with enhancer activity (Pekowska et al., 2011), was reduced in *TFAP2*-KO cells relative to in WT cells (**Fig. 2E'', F''**). While both subsets were strongly enriched for the TFAP2 binding site and certain other binding sites (e.g., RUNX), the subset pioneered by TFAP2 was more strongly enriched for the SOXE and MITF binding sites, while the non-pioneered subset was more strongly enriched for the FRA1, TEAD and the ZFX binding sites (**Fig. 2M, N**). Of note, FRA1 is a pioneer factor (Lee et al., 2018) which could explain why these elements do not depend on TFAP2 to be free of nucleosomes.

Table 1: Hypergeometric analysis: TFAP2 regulated enhancers and gene expression

Regulatory element (Enhancer)	Effect of TFAP2 on H3K27Ac	Effect of TFAP2 on ATAC	Effect of TFAP2 on RNA-seq	N (# of elements)	OR	LB	UB	p-value All DEG's	p-value |Log2FC| >1
-	Activates	-	Activates	3,838	2.36	2.06	2.70	2.8×10^{-33}	1.12×10^{-14}
-	Activates	-	Inhibits	3,838	1.03	0.85	1.24	7.0×10^{-01}	5.9×10^{-01}
-	Inhibits	-	Activates	1,304	1.23	0.93	1.60	1.24×10^{-1}	7.1×10^{-01}
-	Inhibits	-	Inhibits	1,304	2.30	1.87	2.82	4.95×10^{-14}	4.8×10^{-06}
Pioneered	Activates	Activates	Activates	2,002	2.60	2.23	3.06	5.44×10^{-29}	6.3×10^{-20}
Pioneered	Activates	Activates	Inhibits	2,002	1.08	0.80	1.25	9.0×10^{-01}	8.5×10^{-01}
Non-Pioneered	Activates	Independent	Activates	1,836	1.90	1.57	2.30	2.45×10^{-10}	1.0×10^{-06}
Non-Pioneered	Activates	Independent	Inhibits	1,836	1.05	0.82	1.32	6.33×10^{-01}	2.8×10^{-01}
Pioneered	Inhibits	Inhibits	Activates	864	0.68	0.33	1.251	2.9×10^{-01}	1.0×10^{-00}
Pioneered	Inhibits	Inhibits	Inhibits	864	2.33	1.61	3.28	8.08×10^{-06}	9.44×10^{-05}
Non-Pioneered	Inhibits	Independent	Activates	440	1.33	0.83	2.05	0.17	0.83
Non-Pioneered	Inhibits	Independent	Inhibits	440	1.72	1.34	2.43	0.008	0.23

OR: odds ratio, LB: lower boundary, UB: upper boundary, ALL DEGs: all differentially expressed genes (FDR < 0.05) in *TFAP2*-KO clones (two independent clones, 4 replicates each) and WT (4 replicates) SK-MEL-28 cells. Log2FC: Log base 2 fold change. N: numbers of TFAP2 regulated enhancer peaks used in the analysis.

Table 2: Hypergeometric analysis: TFAP2-activated enhancer and promoters, and TFAP2-activated gene expression

Enhancers and promoters	Effect of TFAP2 on H3K27Ac	Effect of TFAP2 on ATAC	Effect of TFAP2 on RNA-seq	N (# of elements)	OR	LB	UB	p-value Log2FC < -1
All peaks	-	-	Activates	36,948	1.66	1.40	1.98	2.4×10^{-08}
TFAP2A (open chromatin)	-	-	Activates	26,373	1.62	1.36	1.92	1.6×10^{-08}
TFAP2A peaks	Activates	-	Activates	4,601	3.11	2.57	3.9	6.0×10^{-24}
TFAP2A peaks	Activates	Independent	Activates	2,324	2.75	2.10	3.55	2.1×10^{-12}
TFAP2A peaks	-	Activates	Activates	5,443	2.58	2.3	2.89	3.9×10^{-27}
TFAP2A peaks	Independent	Activates	Activates	3,241	2.97	2.73	3.70	8.8×10^{-19}
TFAP2A peaks	Activates	Activates	Activates	2,202	4.4	3.46	5.58	4.1×10^{-27}
TFAP2A peaks	Activates OR	Activates	Activates	7,842	3.80	3.1	4.60	1.44×10^{-35}
TFAP2A peaks	Independent	Independent	Activates	19,570	1.55	1.39	1.73	6.1×10^{-02}

OR: odds ratio, LB: lower boundary, UB: upper boundary, Log2FC: Log base 2 fold change. Differentially expressed genes in *TFAP2*-KO clones (two independent clones, 4 replicates each) and WT (4 replicates) SK-MEL-28 cells. N: numbers of TFAP2 regulated enhancer and promoter peaks used in the analysis.

TFAP2A inhibits enhancers by blocking the opening of chromatin

Because of evidence that TFAP2A directly represses gene expression (Lin et al., 2016; Liu et al., 2007; Wong et al., 2012) we next sought to identify candidates for enhancers directly inhibited by TFAP2 paralogs. To this end we filtered promoter-distal TFAP2A peaks for those where the local H3K27Ac signal was higher in *TFAP2*-KO cells than in WT cells (adj. p <0.05, log2FC>1). Analogously to TFAP2-activated enhancers, candidate TFAP2-inhibited enhancers were split between a subset where the ATAC-seq signal was higher in *TFAP2*-KO cells than in WT cells (i.e., TFAP2-inhibited) (**Fig. 2C, G-G'**) and a subset where it was TFAP2-independent (**Fig. 3D, H-H'**). The first subset was significantly associated with TFAP2-inhibited genes (**Fig. 3K**, **Table 1 and Table 3**) and the average H3K4me3 signal at these sites was TFAP2-inhibited (**Fig. 3G''**). Because TFAP2 concomitantly inhibits enhancer activity and chromatin accessibility, we define these enhancers as inhibited by TFAP2 in pioneer factor-mode. The binding site for TFAP2 site was strongly enriched for in these sites, as were those for ETS1 and CTCF (**Fig. 3O**), both transcriptional repressors (Kim et al., 2015; Mavrothalassitis and Ghysdael, 2000). By contrast, the subset of candidate TFAP2-inhibited enhancers where the

282 ATAC-signal was TFAP2-independent was not associated with TFAP2-inhibited
283 genes (**Fig. 3L**, **Table 1**), and the average H3K4me3 signal at them was TFAP2
284 independent (**Fig. 3H''**). We infer these elements are not TFAP2-inhibited
285 enhancers, despite having elevated H3K27Ac signal in TFAP2-KO cells in
286 comparison to WT cells. In conclusion, at TFAP2-inhibited enhancers TFAP2
287 recruits machinery that condenses chromatin and inhibits enhancer activity; the
288 canonical pioneer factor FOXA1 also has this potential (Sekiya and Zaret, 2007;
289 Watts et al., 2011).

Table 3: Hypergeometric analysis: TFAP2-inhibited enhancers and promoters, and TFAP2-inhibited gene expression

Enhancers and promoters	Effect of TFAP2 on H3K27Ac	Effect of TFAP2 on ATAC	Effect of TFAP2 on RNA-seq	N (# of elements)	OR	LB	UB	p-value |Log2FC| >1
TFAP2A (closed chromatin)	-	-	Inhibits	12,931	1.39	1.15	1.69	8.0×10^{-04}
TFAP2A (open chromatin)	-	-	Inhibits	26,373	1.06	0.90	1.25	4.8×10^{-01}
TFAP2A peaks	Inhibits	-	Inhibits	2,830	1.68	1.31	2.13	5.1×10^{-05}
TFAP2A peaks	-	Inhibits	Inhibits	4,236	1.69	1.34	2.12	1.33×10^{-05}
TFAP2A peaks	Inhibits	Inhibits	Inhibits	1,695	2.06	1.51	2.76	8.47×10^{-06}
TFAP2A peaks	Inhibits OR	Inhibits	Inhibits	5,371	1.68	1.38	2.03	3.61×10^{-07}
TFAP2A peaks	Independent	Independent	Inhibited	21,848	0.98	0.82	1.15	7.0×10^{-01}

OR: odds ratio, LB: lower boundary, UB: upper boundary, Log2FC: Log base 2 fold change. Differentially expressed genes in *TFAP2*-KO clones (two independent clones, 4 replicates each) and WT (4 replicates) SK-MEL-28 cells. N: numbers of TFAP2 regulated enhancer and promoter peaks used in the analysis.

290

291 We similarly analyzed whether and how TFAP2 directly activates or directly inhibits
292 promoters. Although TFAP2A peaks are frequently found at promoters (8277 genes
293 have a TFAP2A peak within 1 kb of the TSS), it was uncommon for the underlying
294 H3K27Ac and H3K4Me3 signal to be elevated or reduced in *TFAP2* KO cells relative
295 to in WT cells (119 and 31 candidate for directly activated and directly inhibited
296 promoters, respectively). Similar to the trends for TFAP2-regulated enhancers, the
297 pioneered subset of TFAP2-activated promoters was more strongly associated with
298 TFAP2-activated genes than the non-pioneered subset, and only the pioneered
299 subset of TFAP2-inhibited promoters was associated with TFAP2-inhibited genes
300 (**Supplemental Fig. S6A-L; additional examples in Supplemental Fig. S7A-B**).

301

302 **At additional subsets of MITF peaks overlapping TFAP2A peaks, TFAP2**
303 **facilitates chromatin access for MITF both in pioneer and non-pioneer factor**
304 **modes**

305 A prediction of the TFAP2-as-pioneer-factor model is that binding of transcription
306 factors, like MITF, will depend on TFAP2. Among 37,643 MITF peaks in WT SK-
307 MEL-28 cells that we previously identified by CUT&RUN (Dilshat et al., 2021),
308 15,752 (42%) overlap a TFAP2A peak (i.e., assessed in this study). Of these, 9,413
309 (60%) were within open and active chromatin (**Supplemental Fig. S8A**). To assess
310 MITF binding in the absence of TFAP2 we carried out anti-MITF CUT&RUN in
311 *TFAP2*-KO cell lines. Of note, as *MITF* RNA levels in *TFAP2*-KO cells are only about
312 60% of those in WT cells, an across the board decrease in the average height (read
313 depth) of MITF peaks was possible. Instead, we observed that the average height of
314 MITF peaks not overlapping TFAP2A peaks was equivalent in *TFAP2*-KO cells and
315 in WT (**Supplemental Fig. S8B**). By contrast, among MITF peaks overlapping
316 TFAP2A peaks (15,752), the height of 5,443 (35%) was significantly lower in *TFAP2*-
317 KO cells than in WT cells (adj. $p < 0.05$, log2FC < -1). (**Fig. 3A-D; Supplemental**
318 **Fig. S8C-D and Supplemental Fig. S9**). We refer to these as "TFAP2-dependent
319 MITF peaks," referring only to MITF peaks that appear to be directly TFAP2-
320 dependent (because they overlap TFAP2A peaks in WT cells).

321

322 We reasoned that TFAP2 paralogs could facilitate MITF binding by displacing
323 nucleosomes (i.e., in pioneer factor mode) or alternatively by elevating MITF's affinity
324 for open DNA. Consistent with both models, we observed that TFAP2-dependent
325 MITF peaks were in three subsets with respect to the TFAP2-dependence of the
326 underlying ATAC-seq signal. At about 57% (3,083/5,443) the ATAC-seq signal was
327 significantly lower (**Fig. 3B-C, 3F-F'**), at 37% (2,022/5,443) it was unchanged (**Fig.**
328 **3D, 3G-G'**), and at 6% it was higher (**Fig. 3E, 3H-H'**) in *TFAP2*-KO cells than in WT
329 cells. The first two subsets were strongly associated with TFAP2-activated genes
330 (Hypergeometric test; p-value = 8.4×10^{-26} and p-value = 1.07×10^{-13} respectively)
331 and with MITF-activated genes (Hypergeometric test; p-value = 1.16×10^{-21} and p-
332 value = 4.3×10^{-11} respectively) **(Table 4)**. We infer that at the first subset, TFAP2 is

333 a pioneer factor, facilitating access for MITF and other transcription factors
334 (illustrated in **Fig. 3F''**). Supporting this prediction, the transcription factor binding
335 sites for MITF, SOX10, RUNX and FRA1 were strong enriched at such elements
336 (**Fig. 3F'''**). At the second subset, TFAP2 is a transcriptional activator that recruits
337 MITF, also functioning as a transcriptional activator; we presume another protein
338 serves as a pioneer factor at this subset (illustrated in **Fig. 3G''**). Consistent with this
339 notion, the binding site for JUN, a widely deployed pioneer factor (Vierbuchen et al.,
340 2017), site is strongly enriched in these elements (**Fig. 3G'''**). Examples are shown
341 of TFAP2-dependent MITF peaks near *FRMD4B, CYP7B1, TRPM1 SOX9, EDNRB,*
342 *MREG, GPR143, SNAI2, MEF2C, MYO5A, PAX3, EN1* and *FOXI3* genes (**Fig. 3B-D**
343 **and Supplemental Fig. S8D**). At the third subset of TFAP2-dependent MITF peaks,
344 where ATAC-seq signal was higher in *TFAP2*-KO cells than in WT cells
345 (**Supplemental Fig. S10A-A'**), TFAP2 may serve as a pioneer factor for MITF in
346 MITF's proposed role as transcriptional repressor (Dilshat et al., 2021) (**illustrated in**
347 **Supplemental Fig. S10A''**). However, this category of element was not enriched
348 near genes inhibited by either TFAP2 or MITF (Hypergeometric test; p-value = 6.02 x
349 10^{-02} and p-value = 9.12 x 10^{-02} respectively). These results are consistent with
350 TFAP2 facilitating access for MITF, in its transcriptional activator form, to enhancers
351 in both pioneer-factor and non-pioneer factor modes.

Table 4: Hypergeometric analysis: TFAP2-dependent MITF peaks and gene expression

TFAP2's effect on: MITF	Effect of TFAP2 on ATAC	Effect of TFAP2 on RNA-seq	N (# of elements)	OR	LB	UB	p-value All DEG's	p-value |Log2FC| >1
TFAP2-dependent	-	Activates	5,443	2.96	2.56	3.43	3.47×10^{-41}	8.4×10^{-26}
TFAP2-dependent	-	Inhibits	5,443	1.00	0.81	1.23	9.5×10^{-01}	7.2×10^{-01}
TFAP2-dependent	Activates	Activates	3,083	3.43	2.95	3.98	3.19×10^{-49}	1.16×10^{-26}
TFAP2-dependent	Activates	Inhibits	3,083	1.15	0.92	1.42	1.7×10^{-01}	4.0×10^{-01}
TFAP2-dependent	Independent	Activates	2,358	2.38	1.81	2.55	1.6×10^{-16}	1.07×10^{-13}
TFAP2-dependent	Independent	Inhibits	2,358	1.13	0.91	1.40	2.3×10^{-01}	4.0×10^{-01}
Mutually dependent	Activates	Activates	717	2.967	1.768	4.756	3.47×10^{-05}	9.28×10^{-05}
Mutually dependent	Activates	Inhibits	717	0.789	0.284	1.772	7.07×10^{-01}	1.00
TFAP2-inhibited	Inhibits	Activates	924	0.73	0.48	1.06	1.11×10^{-01}	1.00
TFAP2-inhibited	Inhibits	Inhibits	924	2.75	2.21	3.39	1.1×10^{-17}	3.5×10^{-04}
TFAP2-inhibited	Independent	Activates	681	1.18	0.80	1.68	1.00	1.00
TFAP2-inhibited	Independent	Inhibits	681	2.27	1.72	2.94	2.9×10^{-08}	1.2×10^{-02}

OR: odds ratio, LB: lower boundary, UB: upper boundary, ALL DEGs: all differentially expressed genes in *TFAP2*-KO clones (two independent clones, 4 replicates each) and WT (4 replicates) SK-MEL-28 cells. Log2C: Log base 2 fold change. N: numbers of TFAP2–dependent MITF peaks used in the analysis.

352

353

354 To test for the converse dependence, we carried out anti-TFAP2A CUT&RUN in
355 *MITF*-KO cells. *TFAP2A* mRNA levels were equivalent in *MITF*-KO and WT cells,
356 and the average TFAP2A peak height was globally equivalent by CUT&RUN. At 13%
357 (717/ 5334) of TFAP2-dependent MITF peaks, the TFAP2A peak was, reciprocally,
358 significantly reduced in *MITF*-KO cells (**Fig. 3A, C**). At such loci, the average ATAC-
359 seq was reduced in *TFAP2*-KO cells than in WT cells (**Fig. 3C, 3I-I'**). We termed
360 these peaks mutually-dependent (**illustrated in Fig. 3I''**). Interestingly, mutually-
361 dependent MITF/ TFAP2 peaks were enriched in binding motifs for TFAP2, MITF,
362 BRM2 and TEAD4 but, notably and unlike the other subsets of TFAP2-dependent
363 MITF peaks, not for SOXE (**Fig. 3I'''**). SOX10 co-binds many loci with MITF
364 (Laurette et al., 2015), if SOX10 is absent from mutually-dependent peaks this may
365 explain the dependence of TFAP2 binding on MITF at these sites. At ~40% (288/
366 717) of the mutually dependent peaks, the polycomb repressive histone mark
367 H3K27Me3 was significantly higher (including in the gene body) in *MITF*-KO cells

368 but, unexpectedly, not in *TFAP2*-KO cells, even though MITF binding was lower in
369 *TFAP2*-KO cells **(illustrated in Fig 3I'', Supplemental Fig. 8E-G**).

370 In summary, at about one third of MITF peaks that overlap TFAP2A peaks the MITF
371 binding depends on TFAP2. Such TFAP2-dependent MITF peaks occur both at loci
372 where nucleosome packing depends on TFAP2 (pioneer factor mode) and where it
373 does not (non-pioneer factor mode). At a subset of TFAP2-dependent MITF peaks
374 where TFAP2 acts in pioneer factor mode and characterized by the absence of
375 SOXE binding site TFAP2A binding is, reciprocally, MITF-dependent.

376 **At additional subsets of MITF peaks overlapping TFAP2A peaks, TFAP2**
377 **paralogs inhibit or have no effect on chromatin access for MITF**

378 In Figure 2 we established that at some TFAP2A peaks, TFAP2 paralogs close
379 chromatin, and presumably inhibit binding of transcription factors. Consistent with
380 this prediction, among MITF peaks overlapping TFAP2A peaks, the height of 10%
381 (1,605) was higher in *TFAP2*-KO cells than in WT cells (**Fig. 3A, E; Supplemental**
382 **Fig. S9**). At 58% (924/1,605) of these, the ATAC-seq signal was also significantly
383 higher in *TFAP2*-KO cells versus in WT cells (**violin plot**, **Fig. 3H, H', illustrated in**
384 **Fig. 3H''**). A unique set of transcription factor binding sites, including that for SP1,
385 NFY, JUN and TFE3, were enriched among such elements (**Fig. 3H'''**). Moreover,
386 these elements were modestly associated with TFAP2-inhibited genes**.**

387 Of note, at the majority of MITF peaks that overlap TFAP2A peaks (65%, 10,418/
388 15,752), the height was equivalent in TFAP2-KO and WT cells (**Supplemental Fig.**
389 **S9**). Interestingly TFAP2-independent MITF peaks were not strongly enriched for the
390 TFAP2 binding site (**Supplemental Fig. S11A**), implying that TFAP2 is attracted to
391 many of these sites via other proteins rather than binding directly to the DNA. Such
392 indirect binding may be less avid, as the average height TFAP2-independent MITF
393 peaks was smaller than that of TFAP2-dependent MITF peaks (compare WT MITF
394 signal in (**Supplemental Fig. S9, compare cluster 1 and 4 in WT cells**). As
395 expected, TFAP2-independent MITF peaks were associated neither with TFAP2-
396 activated nor TFAP2-inhibited genes.

397 **TFAP2 and MITF co-regulate genes in the melanocyte gene regulatory network**

398 The delayed pigmentation in zebrafish *tfap2a/tfap2e* double mutants was consistent
399 with two mechanisms which are not exclusive of one another. In the first mechanism,
400 TFAP2 paralogs directly activate *MITF* expression, and thereby indirectly activate
401 expression of pigmentation genes. In the second mechanism, TFAP2 paralogs
402 directly activate expression of pigmentation genes. Supporting the first mechanism,
403 there is a pioneered TFAP2-activated enhancer in intron 2 of the *MITF* gene
404 (**Supplemental Fig. S12**), and *MITF* mRNA levels are about 40% lower in TFAP2-
405 KO cells than in WT cells. However, the first mechanism predicts that loss of TFAP2
406 would most strongly diminish the expression of the most highly MITF-dependent
407 genes. However, many of the genes whose expression was most strongly reduced in
408 *MITF*-KO cells compared to in WT cells were completely TFAP2-independent, or
409 indeed were TFAP2-inhibited (**Supplemental Table 4**). To assess the second
410 mechanism, we identified the set of genes activated directly by MITF, defined as
411 MITF-activated genes associated with an MITF peak, and the set of genes directly
412 activated by TFAP2, defined as TFAP2-activated genes associated with an TFAP2-
413 activated enhancer (i.e., of pioneered or non-pioneered variety). Supporting the
414 second mechanism, genes activated directly both by TFAP2 and by MITF were
415 enriched for GO terms related to pigmentation (**Fig. 4B**), although genes related to
416 pigmentation were among those apparently directly regulated solely by MITF or
417 TFAP2 paralogs (**Fig. 4C**) (Baxter et al., 2019). We took a similar approach to
418 identify genes directly inhibited by TFAP2 and/or by MITF (**Fig. 4D**). Genes directly
419 inhibited by both were strongly enriched for GO terms related to cell adhesion and
420 cell migration (**Fig. 4E**). In summary, reduced expression of pigmentation genes and
421 elevated expression of invasion genes in *TFAP2*-KO cells compared to in WT cells is
422 largely explained by the direct activation and inhibition, respectively, of these
423 categories of genes by TFAP2 paralogs.

424 Considering the strong correlation of TFAP2-inhibited genes with cell migration we
425 performed *in vitro* scratch-recovery-assays and characterized the migrative capacity
426 of our TFAP2-KO cells. Unexpectedly, while WT SK-MEL-28 cells closed the wound
427 after 24 hours, both of our *TFAP2*-KO clones (clone 4.3 and clone 2.12) failed to
428 close the wound within that time (**Supplemental Fig. 13D**). This finding also
429 contrasts with the observation that the expression *tfap2e* correlates negatively with
430 the migratory capacity of zebrafish models of melanoma (Campbell et al., 2021), but

431 it is consistent with the accumulation of melanocytes in the dorsum of zebrafish
432 *tfap2a* knockout embryos (Barrallo-Gimeno et al., 2004; Knight et al., 2004; Knight et
433 al., 2003) and *tfap2a/ tfap2e* double mutant embryos (**Fig. 1, Supplemental Fig.S1**).
434 Furthermore, these results are consistent our previous findings that knocking-down
435 MITF negatively influences cell migration and invasion (Dilshat et al., 2021). The
436 reduced migrative capacity of *TFAP2*-KO cells may be attributed to the strong up-
437 regulation of genes associated with cell adhesion in *TFAP2*-KO cells.

438

439 Finally, we considered how TFAP2 paralogs might regulate the phenotype in
440 melanoma cells. Advanced melanoma is characterized by lower levels of TFAP2A
441 than benign nevi (e.g., Huang et al., 1998), and low transcript levels of *tfap2*
442 paralogs are associated with an invasive phenotype in zebrafish melanoma
443 (Campbell et al., 2021). We examined the association of TFAP2-activated and
444 TFAP2-repressed genes (**Supplemental Fig. 13A-C**) with gene expression profiles
445 from melanoma tumors and melanoma cell lines with distinct phenotypes (Hoek et
446 al., 2008a; Hoek et al., 2006; Jonsson et al., 2010; Rambow et al., 2018; Tirosh et
447 al., 2016; Tsoi et al., 2018; Verfaillie et al., 2015). Enrichment analysis showed (Yu
448 et al., 2012) melanoma profiles previously found to be associated with high levels of
449 MITF activity were enriched for genes directly activated by TFAP2, including the
450 subset associated with TFAP2-dependent MITF peaks (**Fig. 4F**). Moreover,
451 melanoma profiles associated with low levels of MITF activity were enriched for
452 genes directly by TFAP2 (**Fig. 4F**).

453

454 **Discussion**

455

456 In this study, we confirm that Tfap2 paralogs are necessary for timely pigmentation in
457 zebrafish embryos, as well as for normal levels of the expression of pigmentation
458 genes in a melanoma cell line. We also describe how Tfap2 affects expression of
459 such genes, and test the hypothesis that it makes chromatin more accessible to
460 MITF, a transcription factor known to directly regulate the expression of pigmentation
461 genes. The latter involved assessing the consequences of the loss of *MITF* alone,
462 and that of both *TFAP2A* and *TFAP2C*, on global gene expression; on chromatin

463 marks indicative of enhancers, promoters, and repressed chromatin; on nucleosome
464 positioning; and on the binding of TFAP2A to chromatin in *MITF* mutants and that of
465 MITF to chromatin in *TFAP2A/TFAP2C* double mutants. Integration of these
466 datasets yielded a deeper understanding of the mechanisms whereby TFAP2
467 regulates gene expression than could be acquired by more traditional methods.
468
469 Integrating genomic data sets permitted us to identify genomic elements that were
470 bound by TFAP2A in WT cells and that either lost or gained H3K27Ac signal in
471 TFAP2-KO cells; we inferred that these elements were enhancers directly activated
472 or inhibited by TFAP2. Of note, only a minority of TFAP2A peaks coincided with
473 TFAP2-dependent enhancers. As expected by the Tfap2 as pioneer factor model, at
474 a subset of TFAP2A-dependnet enhancers the ATAC-signal was TFAP2-activated.
475 Interestingly, there were elements where the ATAC-seq signal was TFAP2 activated
476 but the H3K27Ac signal independent and such elements were strongly associated
477 with TFAP2-activated genes. It was also interesting that at a subset of TFAP2-
478 inhibited enhancers, loss of TFAP2 led to opening of the chromatin, implying that
479 TFAP2 paralogs recruit distinct transcription factors, and that these in turn recruit
480 either enzymes that open chromatin or enzymes that condense it, in locus-specific
481 fashion. The latter is consistent with findings for FOXA1, which has been shown to
482 recruit proteins that condense chromatin, like GRG3 (Sekiya and Zaret, 2007; Watts
483 et al., 2011).
484
485 A second discovery from our analyses is that TFAP2 can activate enhancers in a
486 non-pioneer factor mode. At a subset of TFAP2A peaks where the H3K27Ac signal
487 was TFAP2-activated, the ATAC-seq signal was TFAP2-independent. Further
488 evidence that such elements are TFAP2-dependent enhancers is that their average
489 H3K4Me3 signal was also TFAP2-dependent. We infer that TFAP2 activates and
490 inhibits these enhancers, but not as a pioneer factor. At such enhancers the
491 continued presence of TFAP2 is necessary for continued acetylation of histone H3
492 lysine 27 (H3K27Ac), which fits with evidence that TFAP2 binds the histone acetyl
493 transferase p300/CBP (Braganca et al., 2003) and inhibits the NURD histone-
494 deacetylase complex (White et al., 2021). TFAP2 may attract other transcription
495 factors without affecting nucleosome positioning; indeed, some TFAP2-dependent
496 MITF peaks were found at Non-pioneered TFAP2- activated enhancers. The fact that

497 the TFAP2 binding site is not strongly enriched at these Non-pioneered TFAP2-
498 activated enhancers may imply that TFAP2 binds these elements indirectly. Finally,
499 we refer to these elements as non-pioneered TFAP2-activated enhancers because
500 in the absence of TFAP2 their activity is lost but chromatin stays open. Our
501 experimental design could not rule out the possibility that TFAP2 stably pioneered
502 these elements such that chromatin remained open (but not active) after TFAP2 was
503 removed. A precedent for this scenario is that at a subset of elements pioneered by
504 PAX7, chromatin remains open after the removal of PAX7 (Mayran et al., 2018).
505 However, the observation that TFAP2 site is less enriched compared to that of
506 pioneered TFAP2-activated enhancers, and that the binding sites of pioneer factors
507 FOS and JUN are enriched (Bejjani et al., 2019), supports the alternative model that
508 such elements are simply pioneered by different transcription factors.
509
510 A third finding from this study is that at a subset of MITF/TFAP2A co-bound peaks,
511 MITF binding was reduced in *TFAP2*-KO cells. A subset of such TFAP2-dependent
512 MITF peaks were present at Pioneered TFAP2-activated enhancers, and at *TFAP2*-
513 independent NDRs (some of which were Non-pioneered TFAP2-activated
514 enhancers, where the mechanism of recruitment of MITF is distinct). Thus, TFAP2
515 modulates MITF activity at certain loci by providing access to chromatin. Of note, at
516 a subset of MITF/TFAP2A peaks, TFAP2 binding was lost in *MITF*-KO cells. There is
517 precedent for reciprocal binding for pioneer factors, in the cases of both FOXA1 and
518 steroid hormone receptors, at subsets of sites where they are co-bound (Swinstead
519 et al., 2016a). Why are all MITF/TFAP2A peaks not mutually dependent? Notably, at
520 many MITF/TFAP2A mutually dependent peaks, the repressive mark H3K27Me3
521 accumulated in MITF-KO cells. This is consistent with evidence a) that the SWI/SNF
522 complex, which MITF probably recruits to such loci, competes for access to
523 chromatin against the Polycomb repressor complex, which deposits H3K27Me3
524 (Wilson et al., 2010), and b) that the binding of pioneer factors is impeded by
525 condensed H3K27me3-positive chromatin (Petruk et al., 2017; Wilson et al., 2010).
526 A possible explanation for this is that at TFAP2-dependent MITF peaks, some
527 measure of BRG1 binding is retained, possibly recruited by another activator like
528 SOX10, in MITF KO cells, but this is not the case for MITF/TFAP2A mutually
529 dependent peaks.
530

531 Finally, our results suggest a mechanism that could account for how TFAP2
532 promotes the pigmentation of embryonic melanophores, the expression of
533 pigmentation genes, and possibly the proliferation of melanoma cells. First, *MITF*
534 expression is lower in *TFAP2*-KO than WT cells. Second, because TFAP2 facilitates
535 binding of MITF to enhancers and promoters of genes that govern pigmentation, the
536 presence of TFAP2 leads to higher expression of those genes. Although the set of
537 MITF-activated but TFAP2-independent genes was not enriched for pigmentation
538 genes, it did include some such genes including *MLANA*, *TYRP1* and *PMEL.*
539 Notably, despite lower MITF mRNA expression in *TFAP2*-KO cells, binding of MITF
540 was unchanged at such genes. This might explain why zebrafish embryonic
541 melanocytes become pigmented more slowly in *tfap2a/tfap2e* double mutants: the
542 number of melanophores in these mutants animals was reduced in embryos
543 depleted for *tfap2a*, singly or in combination with *tfap2e*, and the doubling time of
544 TFAP2-KO cells was longer than that of their WT counterparts. Also, MITF is known
545 to promote proliferation, but whether TFAP2 and MITF cooperate to promote
546 proliferation remains unclear. The expression of genes promoting cell migration and
547 invasion has been observed to be higher in cells with low versus high MITF activity
548 (Rambow et al., 2019). Indeed we show evidence suggesting that TFAP2 paralogs
549 directly suppress such genes, consistent with our previous findings (Campbell et al.,
550 2021). Thus, independent of its other activities as a transcription factor, TFAP2
551 determines which genes can be activated by MITF. In summary, MITF activity in
552 melanoma cells – and thus the phenotypes of these cells – depend in part on the
553 presence of transcription factors that give MITF access to specific regulatory
554 elements.
555
556 **Materials and Methods**
557
558 **Zebrafish lines and maintenance**
559
560 D. rerio were maintained in the University of Iowa Animal Care Facility according to a
561 standard protocol (protocol no. 6011616). All zebrafish experiments were performed
562 in compliance with the ethical regulations of the Institutional Animal Care and Use
563 Committee at the University of Iowa and in compliance with NIH guidelines.

564 Zebrafish embryos were maintained at 28.5℃ and staged by hours or days post-
565 fertilization (hpf or dpf).
566
567
568 **Generation of a zebrafish *tfap2e* loss-of-function allele**
569
570 To generate the tfap2e loss-of-function allele, we designed paired (e.g., left and
571 right) zinc finger nucleases (ZFN) targeting exon 2 of the tfap2e locus resulting in
572 non-homologous end-joining and disruption of the open reading frame for Tfap2e.
573 Briefly, the online tool, ZiFiT (Sander et al., 2010), was used to identify an optimal
574 ZFN target site [utilizing the CoDa approach (Sander et al., 2011). Once identified, a
575 custom DNA fragment encoding the entire left or right zinc finger array (ZFA) along
576 with flanking XbaI and BamHI restriction sites was synthesized (Integrated DNA
577 Technologies, Coralville, IA). Subsequently, the ZFA fragment was subcloned into
578 pMLM290 (Addgene, plasmid 21872), which includes a modified FokI nuclease
579 domain (Miller et al., 2007). Next, the fully assembled ZFN was PCR amplified,
580 directionally cloned into pENTR-D/TOPO (ThermoFisher Scientific), and finally
581 subcloned into pCS2+DEST using Gateway LR Clonase II enzyme mix
582 (ThermoFisher Scientific). Once assembled, the final pCS2+ plasmids were
583 sequence verified, linearized, mRNA synthesized in vitro (mMessage mMachine SP6
584 Kit, Ambion/ThermoFisher Scientific). Synthesized RNA was cleaned using the
585 Qiagen RNeasy Kit (Qiagen) and both left and right ZFN components were co-
586 injected into 1-cell stage zebrafish embryos. Following injections, embryos were
587 initially screened via PCR and restriction enzyme digest to confirm editing at the
588 target site. Upon confirmation, additional embryos from a similar clutch (F0's) were
589 allowed to develop into adulthood, 'mosaics' identified and out-crossed, and a stable
590 F1 generation isolated.
591
592 **Cell lines, reagents, and antibodies**
593
594 The cells referred to as WT throughout the document are the parent SK-MEL-28
595 (HTB-72) line. They and the derivative line, delta6-MITF knockout cells (referred to
596 as MITF-KO cells in this work), were obtained from the laboratory of Dr. Eirikur
597 Steingrimsson. The cells were grown in RPMI 1640 medium (Gibco #5240025)

598 supplemented with 10% FBS (Gibco #10270106) at 5% CO_2 and 37°C. Cells were
599 tested for, and determined to be free of, mycoplasma. SK-MEL-28 cells harbor the
600 $BRAF^{V600E}$ and $p53^{L145R}$ mutations (Leroy et al., 2014). The following primary
601 antibodies and their respective dilutions were used in western blotting (WB) and
602 CUT&RUN experiments: anti-Tubulin (Sigma, #T6199), 1:5000 (WB); anti-MITF
603 (Sigma, #HPA003259), 1:2000 (WB), 1:100 (CUT&RUN); anti-TFAP2A (Abcam,
604 ab108311), 1:5000 (WB), 1:200 (CUT&RUN); anti-TFAP2C (Santa-Cruz #SC-12762
605 X), 1:1000 (WB); anti-H3K27Ac (EMD Millipore, #07-360), 1:100 (CUT&RUN); anti-
606 H3K4Me3 (EMD Millipore, #05-745R), 1:100 (CUT&RUN); H3K27Me3 (EMD
607 Millipore, #07-449), 1:100 (CUT&RUN); Rabbit IgG (EMD Millipore,#12-370), 1:100
608 (CUT&RUN); Mouse IgG (EMD Millipore, #12-371), 1:100 (CUT&RUN). The
609 following secondary antibodies and their respective dilutions were used: Anti-mouse
610 IgG(H+L) DyLight 800 conjugate (Cell Signaling Technologies, #5257), 1:20000; and
611 anti-rabbit IgG(H+L) DyLight 680 conjugate Cell Signaling Technologies, #5366),
612 1:100. Images were captured using an Odyssey CLx Imager (LICOR Biosciences).
613
614
615 **Purification of pA/G-MNase**
616
617 *E.coli* strain BL21-DE3 was transformed with plasmid DNA pAG-MNase-6xHis
618 (Addgene, plasmid #123461). Recombinant pAG-MNase was purified from cells
619 grown in LB medium to OD600 0.6 at 37°C. Cells were induced with 0.5 mM IPTG
620 and cultured for 16 hours at 20°C. Cell pellets were homogenized in lysis buffer (10
621 mM Tris, pH 7.5, 300 mM NaCl, 10 mM imidazole) containing lysozyme and
622 protease inhibitors, then sonicated and the slurry was cleared by centrifugation (35K
623 RPM, Ti70 rotor). The supernatant was subjected to IMAC chromatography (NI-NTA
624 column) and to size-exclusion fractionation (Superdex 75) using a BioLogic DuoFlow
625 QuadTec FPLC system (Bio-Rad). The purified pAG-MNase was concentrated by
626 buffer exchange with ultrafiltration (Amicon Ultra-15, 10K). Finally, the purified pAG-
627 MNase was diluted in dilution buffer (10 mM Tris pH7.5, 120 mM NaCl, 0.01mM
628 EDTA, and 50% glycerol), and stored at -80°C.
629
630 **Generation of *TFAP2A*; *TFAP2C* knockout cell lines (*TFAP2*-KO)**
631

632 *TFAP2*-KO clones were generated using the Alt-R CRISPR-Cas9 technology from
633 Integrated DNA Technologies (IDT). Briefly, crRNAs targeting exon 2 of *TFAP2A* and
634 *TFAP2C* were designed using the Cas9 guide RNA design checker tool (crRNA
635 sequences below). Equimolar concentrations of crRNA and tracrRNA (IDT,
636 #1072532) were annealed to form gRNA complexes. The ribonucleoprotein (RNP)
637 complex was prepared by mixing gRNAs and Cas9 protein (IDT #1081058). SK-
638 MEL-28 cells were transfected with constructs encoding components of RNP
639 complexes using the Lipofectamine CRISPRmax Cas9 transfection reagent
640 (ThermoFisher #CMAX00015) following the manufacturer's protocol. Single-cell
641 colonies were screened by PCR and Sanger sequencing using primers flanking the
642 cut sites (primer sequences below). Mutant clones (clone 2.12 and clone 4.3) were
643 selected and further screened by western blotting, using anti-TFAP2A and anti-
644 TFAP2C antibodies. The control cell lines used in this study were generated
645 following this protocol but without adding gRNA duplexes.
646
647

crRNA	**Sequence (5'-3')**
TFAP2A_ex2_gRNA1	CGTCACGACGGCACCAGCAAGTTTTAGAGCTATGCT
TFAP2A_ex2_gRNA2	CTTACCTCACGCCATCGAGGGTTTTAGAGCTATGCT
TFAP2C_ex2_gRNA1	CGCCACGACGGGAGCAGCAAGTTTTAGAGCTATGCT
TFAP2C_ex2_gRNA2	CCACGACATGCCTCACCAGAGTTTTAGAGCTATGCT
Primers	**Sequence (5'-3')**
TFAP2A_geno_Fw	TCTCTTGTGCCCCCTCCATA
TFAP2A_geno_Rv	GCCCACCGACTGTATGTTCCA
TFAP2C_geno_Fw	CCGTGACCCCGATTTTGGAT
TFAP2C_geno_Rv	CGGCTTCACAGACATAGGCA

648
649
650 **SDS-PAGE and Western blotting**
651
652 *TFAP2*-KO and WT cells were washed in ice-cold PBS. RIPA buffer containing
653 protease inhibitors (Roche, cOmplete Mini) was added and cells were lysed on ice
654 for 20 minutes. Cell lysates were centrifuged at 14,000 g for 20 minutes and the
655 quantity of protein in the supernatants was quantified using Bradford assays (Bio-

656 Rad #5000002). Laemmli sample buffer (Bio-Rad #1610747, 5% 2-mercaptoethanol)
657 was added to 20 µg protein and samples were boiled at 95°C for 5 minutes before
658 being loaded onto a 10% SDS-polyacrylamide gel (Bio-Rad #4568034). Protein was
659 transferred to polyvinylidene fluoride (PVDF) membranes (Thermo Scientific
660 #88520), which were incubated overnight with primary antibody. Membranes were
661 washed 3 times with TBS-T and incubated with horseradish peroxidase-conjugated
662 anti-rabbit or anti-mouse for 1 hour at room temperature, washed, and imaged using
663 an Amersham Imager 600.
664
665
666
667
668 **ATAC-seq**
669
670 ATAC-seq was performed according to (Buenrostro et al., 2015; Liu et al., 2020) with
671 minor alterations. Briefly, 70,000 *TFAP2*-KO cells (clone 2.12 and clone 4.3, four
672 replicates each) and WT cells (four replicates) were lysed in ice-cold lysis buffer (10
673 mM Tris-HCl, pH 7.4, 10 mM NaCl, 3 mM MgCl2, 0.1% NP-40: Sigma).
674 Transposition was performed directly on nuclei using 25 µl tagmentation reaction mix
675 (Tagment DNA Buffer #15027866, Tagment DNA Enzyme #15027865 from Illumina
676 Tagment DNA kit #20034210). Tagged DNA was subjected to PCR amplification and
677 library indexing, using the NEBNext High-Fidelity 2x PCR Master Mix (New England
678 Biolabs #M0451S) with Nextera DNA CD Indexes (Illumina #20015882), according to
679 the following program: 72℃ for 5 minutes; 98℃ for 30 seconds; 12 cycles of 98℃ for
680 10 seconds, 63℃ for 30 seconds, and 72℃ for 1 minute. The PCR product was
681 purified with 1.8 times the volume of Ampure XP beads (Beckman Coulter #A63881).
682 Library quality was assessed using a BioAnalyzer 2100 High Sensitivity DNA Chip
683 (Agilent Technologies). All DNA libraries that exhibited a nucleosome pattern were
684 pooled and processed for 150bp paired-end sequencing.
685
686
687 **ATAC-seq peak calling and differential analysis**
688

689 ATAC-seq was performed using 150 bp paired-end sequencing reads. Raw ATAC-
690 seq reads were trimmed using Trim Galore Version 0.6.3 (Developed by Felix
691 Krueger at the Babraham Institute) and aligned to human genome assembly hg19
692 (GRCh37) using Bowtie 2 (Langmead and Salzberg, 2012; Langmead et al., 2009)
693 with default parameters. Sorting, removal of PCR duplicates, and identification of
694 fragments shorter than 100 bp as the nucleosome-depleted-regions (NDRs), was
695 performed using BAM filter version 0.5.9. DeepTools version 3.3.0 (Ramírez et al.,
696 2016) was used to check the reproducibility of the biological replicates and generate
697 bigWig coverage files for visualization. Peaks were called using model-based
698 analysis of ChIP-seq 2 (MACS2, version 2.1.1.20160309.6) (Zhang et al., 2008).
699 NDRs for which accessibility differed between *TFAP2*-KO and WT cells were
700 identified using DiffBind version 2.10 (Ross-Innes et al., 2012) with log2 fold-change
701 threshold of >1 and a false discovery rate (FDR) < 0.05. NDRs that are directly
702 regulated by TFAP2 were identified by overlapping differentially accessible NDRs
703 with anti-TFAP2A CUT&RUN peaks; a 1-bp window was used to define overlap.
704 Peaks were assigned to genes using GREAT with a peak-to-gene association rule of
705 the nearest-gene-within-100 kb (McLean et al., 2010). Both the raw ATAC-seq files
706 and processed sequencing data presented in this manuscript have been deposited in
707 the Gene Expression Omnibus (GEO) repository (GSE number pending).
708
709
710 **CUT&RUN**
711
712 CUT&RUN sequencing was performed in *TFAP2*-KO cells (clone 2.12 and clone 4.3,
713 two replicates each) and WT cells (two replicates) as previously described (Meers et
714 al., 2019; Skene and Henikoff, 2017), but with minor modifications. Cells in log-
715 phase culture (approximately 80% confluent) were harvested by cell scraping,
716 centrifuged at 600 g (Eppendorf, centrifuge 5424) and washed twice in calcium-free
717 wash-buffer (20 mM HEPES, pH7.5, 150 mM NaCl, 0.5 mM spermidine, and
718 protease inhibitor cocktail cOmplete Mini, EDTA-free from Roche). Pre-activated
719 concanavalin A-coated magnetic beads (Bangs Laboratories, Inc) were added to cell
720 suspensions ($2x10^5$ cells) and incubated for 15 minutes at 4ºC. Antibody buffer
721 (wash-buffer with 2mM EDTA and 0.05% digitonin) containing anti-TFAP2A, anti-
722 MITF, anti-H3K4Me3, anti-H3K27Me3, anti-H3K27Ac or Rabbit IgG was added and

723 cells were incubated overnight at 4ºC. Cells were washed in dig-wash buffer (wash
724 buffer containing 0.03% digitonin), and pAG-MNase was added at a concentration of
725 500 µg/mL. The pAG-MNase reactions were quenched with 2X Stop Buffer (340mM
726 NaCl, 20mM EDTA, 4mM EGTA, 0.05% digitonin, 100 µg/mL RNAse A (10 mg/mL,
727 Thermo Fisher Scientific #EN0531), 50 µg/mL glycogen (20mg/mL, Thermo Fisher
728 Scientific #R0561) and 2 pg/mL sonicated yeast spike-in control). Released DNA
729 fragments were treated with 1µL/mL phosphatase K (20mg/mL, Thermo Fisher
730 Scientific #25530049) for 1 hour at 50ºC and purified by phenol/chloroform-extraction
731 and ethanol-precipitation. Fragment sizes were analyzed using a 2100 Bioanalyzer
732 (Agilent).
733
734 **CUT&RUN library preparation and data analysis**
735
736 CUT&RUN libraries were prepared using the KAPA Hyper Prep Kit (Roche). Quality
737 control post-library amplification consisted of fragment analysis using the 2100
738 Bioanalyzer (Agilent). Libraries were pooled, brought to equimolar concentrations,
739 and sequenced with 150 bp paired-end reads on an Illumina HiSeq X platform
740 (Novogene, Sacramento, CA). For quality control, paired-end FASTQ files were
741 processed using FastQC (Babraham Bioinformatics). Reads were trimmed using
742 Trim Galore Version 0.6.3 (Developed by Felix Krueger at the Babraham Institute)
743 and then mapped against the hg19 genome assembly using Bowtie2 version 2.1.0
744 (Langmead and Salzberg, 2012; Langmead et al., 2009). The mapping parameters
745 and peak calling of MACS2 peaks (Zhang et al., 2008) were performed as previously
746 described (Meers et al., 2019; Skene and Henikoff, 2017) against their matching
747 control IgG samples. Differential analysis of H3K27Ac and of H3K27Me3 signal in
748 WT and *TFAP2*-KO cells was preformed using MACS2 with a Log2 fold-change
749 threshold of 1, and p-value < 1×10^{-5}. Differential H3K4Me3, MITF and TFAP2A
750 signal in WT, *TFAP2*-KO and when mentioned *MITF*-KO cells was determined using
751 DiffBind version 2.10.0 (Ross-Innes et al., 2012) with a Log2 fold-change threshold
752 of 1, and FDR < 0.05. DeepTools version 3.3.0 was used to check the reproducibility
753 of the biological replicates, to generate bigwig normalized (RPKM) coverage files for
754 visualization and to plot average CUT&RUN-seq and ATAC-seq profiles (-plotProfile)
755 and generate heatmaps (-plotHeatmap) of normalized reads (Ramírez et al., 2016).
756 MultiBigwigSummary was used to extract read counts (-outRawCounts) (Ramírez et

757 al., 2016) and Prism was used to generate Violin and Box plots. Peaks were
758 assigned to genes using GREAT with a peak-to-gene association rule of the nearest-
759 gene-within-100 kb (McLean et al., 2010)
760
761
762
763 **RNA-seq**
764
765 Four replicate RNA-seq experiments were performed on *TFAP2*-KO cells (clone 2.12
766 and clone 4.3) and WT cells. Total RNA was extracted by direct cell lysis using the
767 RNeasy Plus Mini Kit with QiaShredder (Qiagen #47134). RNA samples with an
768 RNA integrity number (RIN) above nine were used for library generation and 150 bp
769 paired-end sequencing on the Illumina HiSeq2500 platform (Novogene, Sacramento,
770 CA). FASTQ sequence files were processed using FastQC (Babraham
771 Bioinformatics) for quality control, and reads were trimmed using Trim Galore
772 Version 0.6.3 (Developed by Felix Krueger at the Babraham Institute) and
773 subsequently aligned to human genome assembly hg19 (GRCh37) using STAR
774 (Dobin et al., 2013). The output of the --quantMode GeneCounts function of STAR
775 was used for the calculation of differential transcript expression using DESeq2 (Love
776 et al., 2014).The rlog function was used to generate log2-transformed normalized
777 counts. Adjusted p-value < 0.05 was used as the threshold for statistically significant
778 differences. Functional enrichment analyses was performed using PANTHER (Mi et
779 al., 2021). A full list of genes differentially expressed between *TFAP2*-KO and WT
780 cells is provided in Supplemental Table 1-3.
781
782 **Motif analyses**
783
784 Both de novo and known motifs were identified within 200 bp of TFAP2-activated
785 and TFAP2-inhibited enhancer and promoter peak summits using HOMER (-
786 findMotifsGenome).
787
788 **Statistical analysis**
789

790 Fisher's Exact Test was used to assess TFAP2-regulated elements (enhancers and
791 promoters) with TFAP2-regulated gene expression. Data processing and analysis
792 was performed in R and the code can be found at
793 https://GitHub.com/ahelv/Differential_Expression. GraphPad-Prism was used to
794 perform Students t-test as indicated in the figure legends
795
796 **Wound scratch assay**
797
798 A total of 500K cells were seeded per well of 6-well plate (Thermo Scientific, #
799 1483210) to reach confluent monolayer. Cells were incubated in serum free media
800 for 6 hours before wounding with a 200 µL pipette tip. Scratches were manually
801 imaged on an inverted light microscope (Leica #10445930) every 6 hours over a 24-
802 hour time period. The distance of scratch closure between WT and *TFAP2*-KO cells
803 were analyzed with Image J software.
804
805 **Acknowledgements**
806 This work was supported by grants from the National Institutes of Health (NIH) to
807 RAC (R01-AR062457), and a postdoctoral fellowship from the American Association
808 for Anatomy (CK). The ES laboratory is supported by grants 207067 and 217768
809 from the Research Fund of Iceland.
810
811 **Author Contributions**
812
813 Conceptualization: CK, RAC.
814 Formal analysis: CK, RD.
815 Funding acquisition: CK, ES, RAC.
816 Investigation: CK, RAC.
817 Methodology: CK, RD, HS, EVO, AH, GB.
818 Statistical analysis: CK, AH.
819 Supervision: ES, RAC.
820 Writing – original draft: CK, RAC.

Fig 1

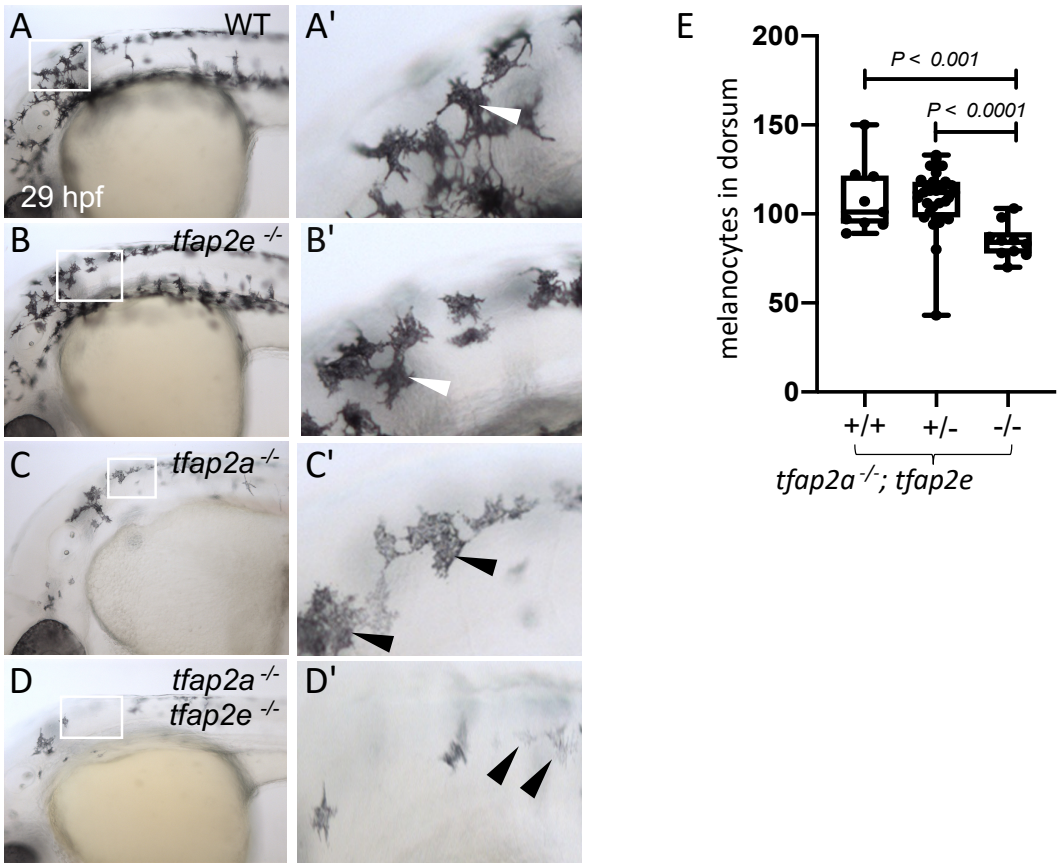

821
822
823

Fig. 2

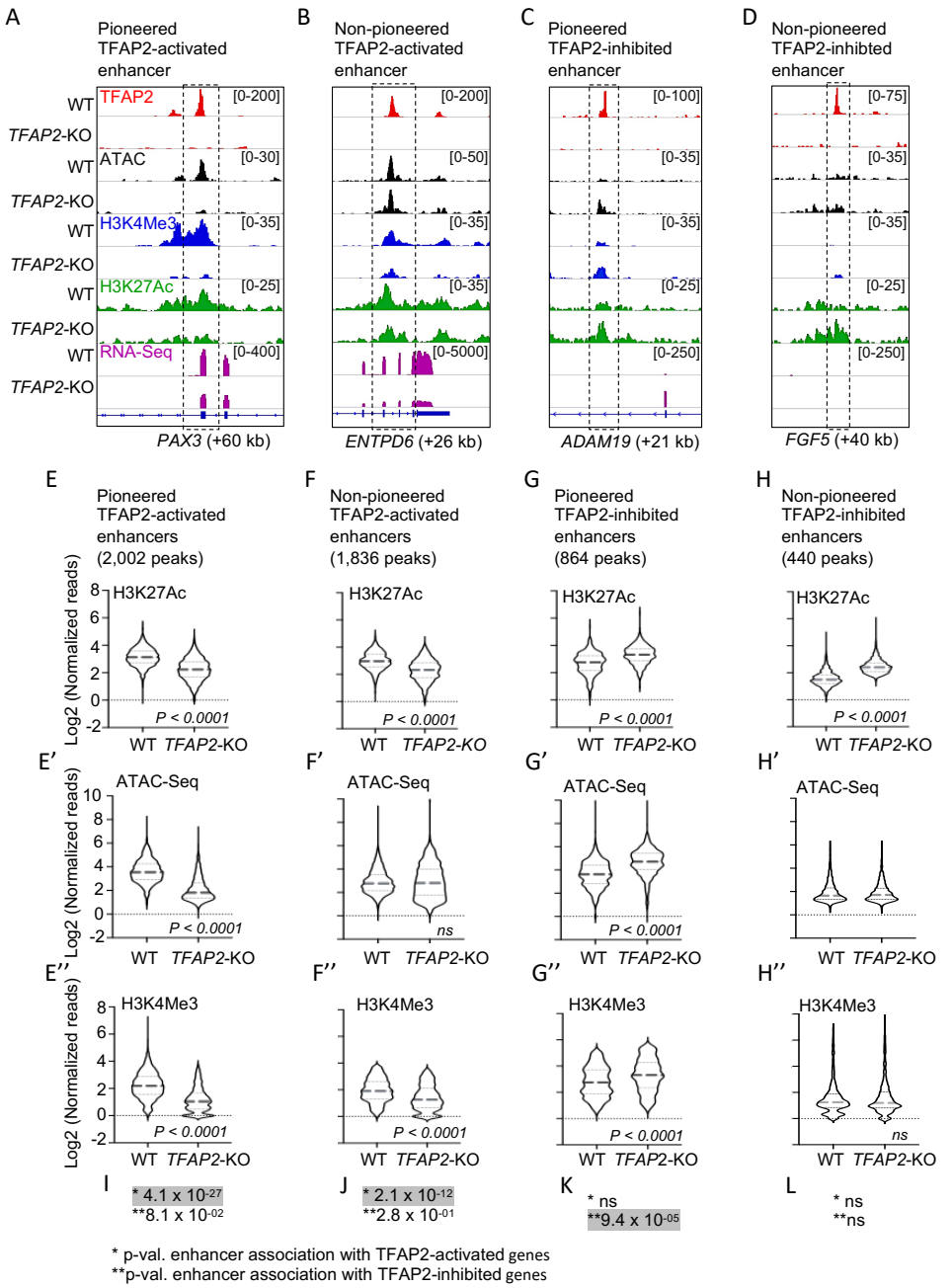
A
Pioneered TFAP2-activated enhancer
B
Non-pioneered TFAP2-activated enhancer
C
Pioneered TFAP2-inhibited enhancer
D
Non-pioneered TFAP2-inhibted enhancer
WT
TFAP2-KO
TFAP2
ATAC
H3K4Me3
H3K27Ac
RNA-Seq
[0-200]
[0-30]
[0-35]
[0-25]
[0-400]
[0-50]
[0-5000]
[0-100]
[0-250]
[0-75]
PAX3 (+60 kb)
ENTPD6 (+26 kb)
ADAM19 (+21 kb)
FGF5 (+40 kb)
E
Pioneered TFAP2-activated enhancers (2,002 peaks)
F
Non-pioneered TFAP2-activated enhancers (1,836 peaks)
G
Pioneered TFAP2-inhibited enhancers (864 peaks)
H
Non-pioneered TFAP2-inhibited enhancers (440 peaks)
Log2 (Normalized reads)
H3K27Ac
ATAC-Seq
H3K4Me3
P < 0.0001
ns
WT TFAP2-KO
I
* 4.1 x 10-27
**8.1 x 10-02
J
* 2.1 x 10-12
**2.8 x 10-01
K
* ns
**9.4 x 10-05
L
* ns
**ns
* p-val. enhancer association with TFAP2-activated genes
**p-val. enhancer association with TFAP2-inhibited genes
M
Pioneered TFAP2-activated enhancers
Motif TF Rank P-value
TFAP2 1,2 1 x 10-600
EBF 3 1 x 10-51
SOXE 4,6 1 x 10-36
RUNX 7 1 x 10-31
MITF 28 1 x 10-12
N
Non-pioneered TFAP2-activated enhancers
Motif TF Rank P-value
TFAP2 1 1 x 10-280
FRA1 2 1 x 10-46
RUNX 4 1 x 10-27
TEAD 6 1 x 10-24
ZFX 7 1 x 10-22
O
Pioneered TFAP2-inhibited enhancers
Motif TF Rank P-value
TFAP2 1,2 1 x 10-63
RUNX 3 1 x 10-37
CST6 4 1 x 10-21
ETS1 6 1 x 10-14
CTCF 12 1 x 10-12

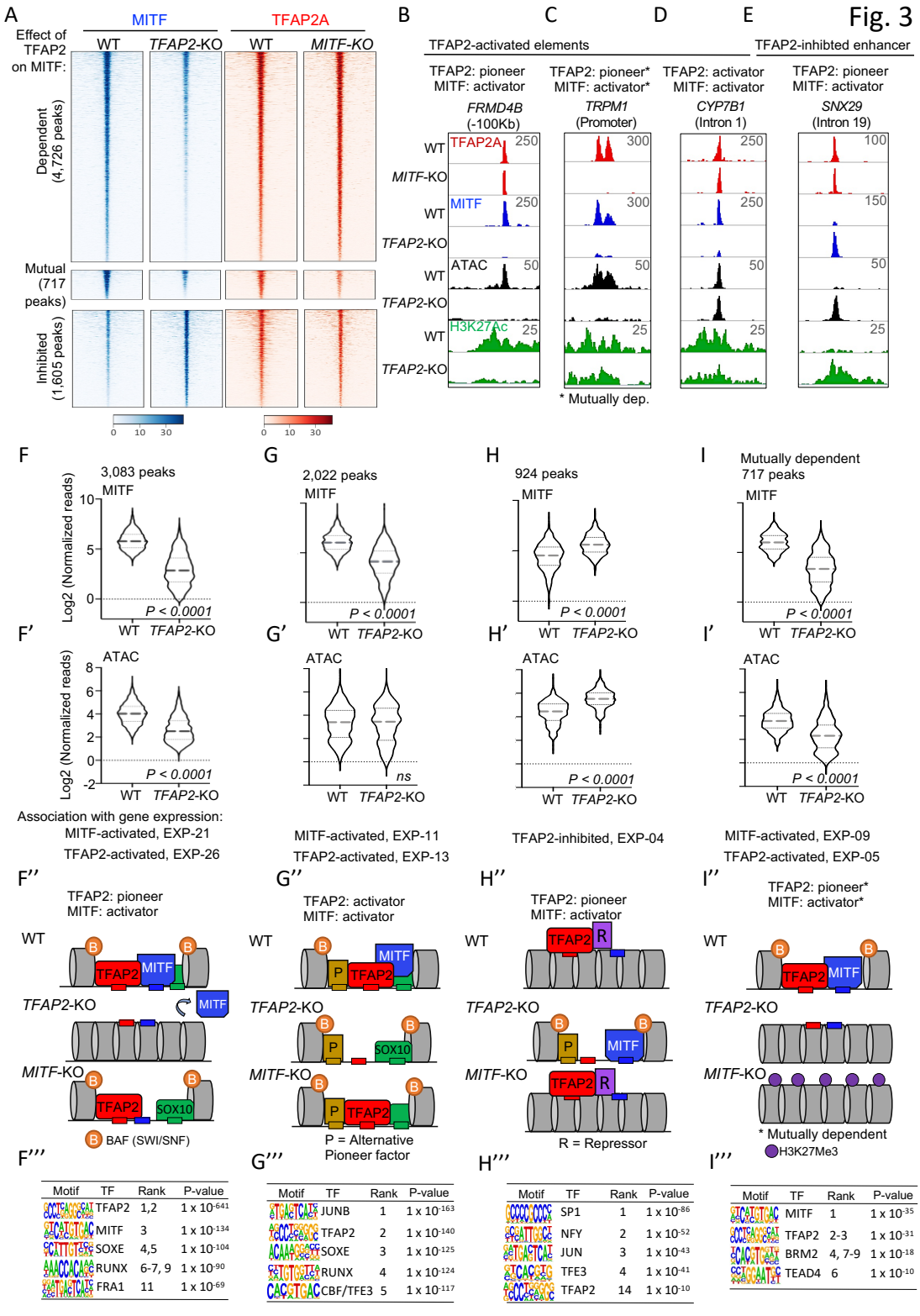
Fig. 3
A
MITF
TFAP2A
Effect of TFAP2 on MITF:
WT
TFAP2-KO
WT
MITF-KO
Dependent (4,726 peaks)
Mutual (717 peaks)
Inhibited (1,605 peaks)
B
C
D
E
TFAP2-activated elements
TFAP2-inhibted enhancer
TFAP2: pioneer MITF: activator
TFAP2: pioneer* MITF: activator*
TFAP2: activator MITF: activator
TFAP2: pioneer MITF: activator
FRMD4B (-100Kb)
TRPM1 (Promoter)
CYP7B1 (Intron 1)
SNX29 (Intron 19)
TFAP2A
MITF
ATAC
H3K27Ac
* Mutually dep.
F
G
H
I
3,083 peaks
2,022 peaks
924 peaks
Mutually dependent 717 peaks
Log2 (Normalized reads)
P < 0.0001
F'
G'
H'
I'
ATAC
ns
Association with gene expression:
MITF-activated, EXP-21
TFAP2-activated, EXP-26
MITF-activated, EXP-11
TFAP2-activated, EXP-13
TFAP2-inhibited, EXP-04
MITF-activated, EXP-09
TFAP2-activated, EXP-05
F''
G''
H''
I''
TFAP2: pioneer MITF: activator
TFAP2: activator MITF: activator
TFAP2: pioneer* MITF: activator*
BAF (SWI/SNF)
P = Alternative Pioneer factor
R = Repressor
* Mutually dependent
H3K27Me3
F'''
G'''
H'''
I'''
Motif TF Rank P-value
TFAP2 1,2 1 x 10-641
MITF 3 1 x 10-134
SOXE 4,5 1 x 10-104
RUNX 6-7, 9 1 x 10-90
FRA1 11 1 x 10-69
JUNB 1 1 x 10-163
TFAP2 2 1 x 10-140
SOXE 3 1 x 10-125
RUNX 4 1 x 10-124
CBF/TFE3 5 1 x 10-117
SP1 1 1 x 10-86
NFY 2 1 x 10-52
JUN 3 1 x 10-43
TFE3 4 1 x 10-41
TFAP2 14 1 x 10-10
MITF 1 1 x 10-35
TFAP2 2-3 1 x 10-31
BRM2 4, 7-9 1 x 10-18
TEAD4 6 1 x 10-10

Fig. 4

A

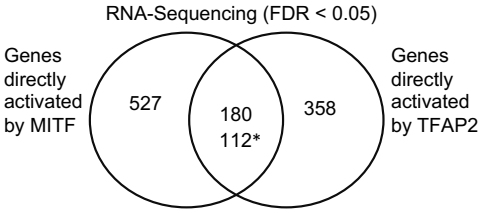

*Associated with a TFAP2-dependent MITF peak

D

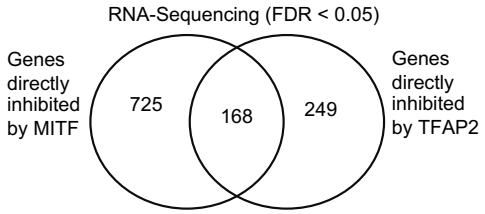

B

MITF and TFAP2-activated genes (Top 5 hits)

GO biological process	Enrichment	No. of genes	FDR
Pigmentation	16.75	11	2.79×10^{-06}
Pigment differentiation	28.02	6	9.79×10^{-04}
Cell differentiation	44	77	8.7×10^{-03}
Cellular pigmentation	13.49	5	4.68×10^{-02}
Receptor signaling	3.51	15	3.78×10^{-02}

E

MITF and TFAP2-inhibited genes (Top 5 hits)

GO biological process	Enrichment	No. of genes	FDR
Vasculature development	6.8	32	1.8×10^{-12}
Tube development	5.13	36	1.4×10^{-10}
Cell motility	4.81	34	2.2×10^{-08}
Cell migration	3.51	31	3.7×10^{-07}
Cell adhesion	3.5	20	7.0×10^{-06}

C

Pigmentation related genes directly activated by:

MITF	**MITF and TFAP2**	**TFAP2**
DKC1	*RAB1A*	*IGFBP7*
MLANA	*RAB32*	*KCTD15*
EIF3B	*HPS3*	*ABCA12*
KBTBD8	*CLCN7*	*CHD7*
RAB27A	*CTNNB1*	*EDNRB*
STX3	*CTSD*	*EN1*
AFG3L2	*DCT*	*HIPK2*
BNC2	*ETS1*	*HTRA1*
CCT2	*GPR143*	*MCM4*
DTNBP1	*MAFB*	*MYO5A*
IRF4	*MFSD12*	*PARN*
MLPH	*MITF*	*PAX3*
MYO10	*MREG*	*RAD21*
OSTM1	*NR4A3*	*SDC2*
PARD3	*OCA2*	*SLC2A11*
PMEL	*PEPD*	*SOX9*
PPARGC1A	*RAB38*	*SYTL2*
PSEN2	*SH3BP4*	*TFAP2C*
RPS14	*SH3PXD2A*	*ALCAM*
RPS7	*SNAI2*	*BLM*
SCUBE2	*TRPM1*	*DISC1*
SLC45A2	*VDR*	*ERBB3*
STXBP1		*FANCC*
SZT2		*LYST*
TYRP1		*MIB1*
USF2		*NBN*
VPS18		*PMCH*
		PRKDC
		SOX5

F

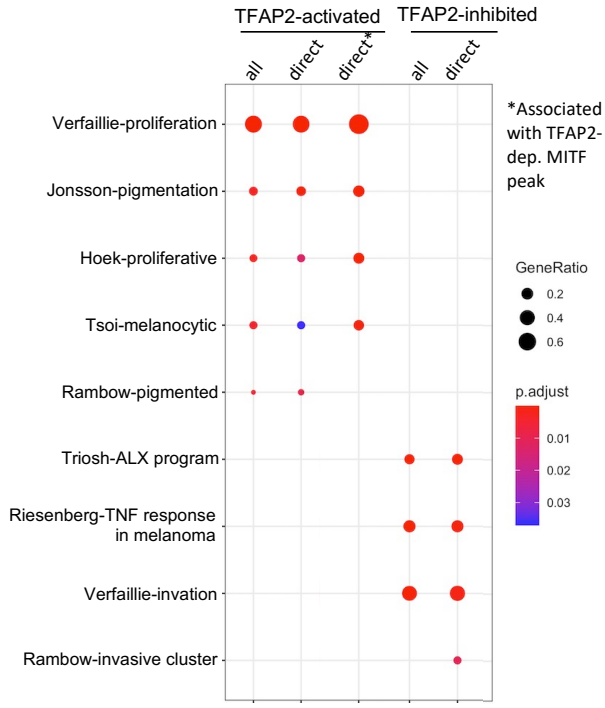

830

831

832 **Figure legends**

833

834 **Figure 1: Stable KO of *tfap2e* has no effect on pigmentation in WT embryos but**
835 **alters melanocyte development and delays melanin synthesis in *tfap2a***
836 **mutants. (A-D)** Lateral views of head and trunk of live embryos at 29 hpf, anterior to
837 the left and dorsal to the top. **(A-A')** A WT (sibling) embryo with normal melanocytes
838 (white arrowhead). **(B-B')** A *tfap2e*$^{ui157ui/157}$ embryo, with melanocytes that are normal
839 in terms of number, differentiation and pigmentation (white arrowhead). **(C-C')** A
840 *tfap2a*$^{low/low}$ homozygous mutant embryo, with fewer melanocytes than its
841 *tfap2e*$^{157/157}$ and WT sibling embryos. **(D-D')** A *tfap2a*$^{low/low}$*; tfap2e*$^{157/157}$ double-
842 mutant embryo, with fewer melanin-producing melanophores than its *tfap2a*$^{low/low}$
843 sibling. **(E)** Box plot illustrating the number of pigmented melanocytes in the dorsum
844 of WT (+/+), *tfap2a* mutant, *tfap2e* mutant, and double *tfap2a; tfpa2e* mutant
845 embryos at 36 hpf. Center line, mean; box limits, upper and lower quartiles;
846 whiskers, minimum and maximum values; black dots, number of melanocytes per
847 individual embryo (WT; n=9, *tfap2a*$^{low/low}$*;tfap2e*$^{+/157}$, n=32; *tfap2a*$^{low/low}$*;tfap2e*$^{157/157}$,
848 n=10). P-value according to the Student's t-test.

849

850 **Figure 2: TFAP2 paralogs facilitate gene expression by opening and**
851 **condensing chromatin. (A-D)** Screenshot of IGV genome browser
852 (GRCH37/hg19), visualizing anti-TFAP2A CUT&RUN-seq (red), ATAC-seq (black),
853 anti-H3K4Me3 CUT&RUN-seq (blue), anti-H3K27Ac CUT&RUN-seq (green) and
854 RNA-seq (magenta) datasets at **(A)** a pioneered TFAP2-activated enhancer at the
855 *PAX3* (+60 kb) locus **(B)** a non-pioneered TFAP2A-activated enhancer at the
856 *ENTPD6* (+26kb) locus **(C)** a pioneered TFAP2-inhibited enhancer at the *ADAM19*
857 (+21 kb) locus and **(D)** a non-pioneered TFAP2A-inhibited enhancer at the *FGF5*
858 (+40kb) locus. Genotypes as labeled; y-axes are grouped scaled per dataset. **(E-E'')**
859 Violin plots representing **(E)** anti-H3K27Ac (two independent replicates) **(E')** ATAC-
860 seq (four independent replicates) and **(E'')** anti-H3K4Me3 (two independent
861 replicates) normalized reads at pioneered TFAP2-activated enhancers. **(F-F'')** Violin
862 plots representing **(F)** anti-H3K27Ac **(F')** ATAC-seq and **(E'')** anti-H3K4Me3
863 normalized reads at non-pioneered TFAP2-activated enhancers. **(G-G'')** Violin plots

representing **(G)** anti-H3K27Ac **(G')** ATAC-seq and **(G'')** anti-H3K4Me3 normalized reads at pioneered TFAP2-inhibited enhancers. **(H-H'')** Violin plots representing **(H)** anti-H3K27Ac **(H')** ATAC-seq and **(H'')** anti-H3K4Me3 normalized reads at non-pioneered TFAP2-inhibited enhancers. P-values shown were determined by Students t-test. **(I-L)** Hypergeometric analysis of TFAP2 regulated enhancers at TFAP2-activated (*) and TFAP2-inhibited (**) genes in *TFAP2*-KO cells (FDR < 0.05, |log2FC| > 1). **(M-O)** Enrichment of transcription factor motifs at (M) pioneered TFAP2-activated enhancers, at (N) non-pioneered TFAP2-activated enhancers and at (O) pioneered TFAP2-inhibited enhancers as determined using HOMER motif analysis. P values were calculated using ZOOPS scoring (zero or one occurrence per sequence) coupled with hypergeometric enrichment analysis. TF; transcription factor.

Figure 3: TFAP2 paralogs facilitate chromatin access by MITF. (A) Density heatmaps of anti-MITF CUT&RUN-seq in SK-MEL-28 and *TFAP2*-KO cells, and anti-TFAP2 CUT&RUN-seq in SK-MEL-28 and *MITF*-KO cells at TFAP2-dependent MITF peaks (top), mutually dependent peaks (center) and TFAP2-inhibited MITF peaks (bottom). Number of peaks in each group as labelled. Regions shown are +/- 3 kb from peak center, normalized reads (RPKM). **(B-E)** Screenshot of IGV genome browser (GRCH37/hg19), showing anti-TFAP2A (red) CUT&RUN-seq in SK-MEL-28 and *MITF*-KO cells, and anti-MITF (blue) CUT&RUN-seq, ATAC-seq (black) and anti-H3K27Ac (green) CUT&RUN-seq profiles in SK-MEL-28 and *TFAP2*-KO cells. Examples of MITF binding at **(B-D)** TFAP2-activated and **(E)** TFAP2-inhibted regulatory elements. Genotypes as labeled; y-axes are grouped scaled per dataset. **(F-F')** Violin plot representing **(F)** anti-MITF CUT&RUN-seq (two independent replicates) and **(F')** ATAC-seq (four independent replicates) at 3,083 pioneered TFAP2-activated MITF peaks. **(G-G')** Violin plot representing **(G)** anti-MITF CUT&RUN-seq and **(G')** ATAC-seq at 2,022 non-pioneered TFAP2-activated MITF peaks. **(H-H')** Violin plot representing **(H)** anti-MITF CUT&RUN-seq and **(H')** ATAC-seq at 924 pioneered TFAP2-inhibited MITF peaks and **(I-I')** Violin plot representing **(I)** anti-MITF CUT&RUN-seq and **(I')** ATAC-seq at 717 mutually dependent peaks. P-value according to Students t-test, ns; not statistically significant, normalized reads RPKM. Association with gene expression; hypergeometric analysis of TFAP2-depednent and TFAP2-inhibited MITF peaks are shown at TFAP2-activated and

898 MITF-activated genes (FDR < 0.05, log2FC > |1|). **(F''- I'')** Schematic representation
899 of TFAP2-dependent and TFAP2-inhibited MITF peaks as labelled; B; BAF complex
900 (SWI/SNF), P; alternative pioneer factor. R; repressor protein. Transcription factor
901 binding sites indicated by small rectangles, TFAP2 (red), MITF (blue) and alternative
902 pioneer factor (yellow), example activator SOX10 (green) . **(F''' – I''')** Enrichment of
903 transcription factor motifs using HOMER at (F''') pioneered TFAP2-dependent MITF
904 peaks, (G''') non-pioneered TFAP2-dependent MITF peaks, (H''') TFAP2-inhibited
905 MITF peaks and **(I''')** mutually dependent peaks. P values were calculated using
906 ZOOPS scoring (zero or one occurrence per sequence) coupled with hypergeometric
907 enrichment analysis. TF; transcription factor.
908
909 **Figure 4: TFAP2 and MITF co-regulate pigmentation and cell differentiation**
910 **genes in SK-MEL-28 cell lines. (A)** Venn diagram representing directly MITF
911 activated genes (MITF peaks within 100Kb of a TSS), based on RNA-seq, in *MITF*-
912 KO verses WT cells (FDR < 0.05) and genes directly activated by TFAP2 (TFAP2-
913 activated enhancers within 100Kb of a TSS), based on RNA-seq, with TFAP2-
914 activated enhancers, in *TFAP2*-KO verses WT cells (FDR < 0.05). The number of
915 overlapping genes with TFAP2-dependent MITF peaks are also shown (*). **(B)** Gene
916 ontology (GO) biological process analysis (Top 5 hits) that are enriched among
917 MITF- and TFAP2-activated genes. **(C)** A curated list of pigment-associated genes
918 (Baxter et al., 2009) was intersected with directly MITF-activated, directly
919 MITF/TFAP2-activated, and TFAP2-acitvated genes and represented by gene list.
920 **(D)** Venn diagram representing directly MITF inhibited genes, based on RNA-seq, in
921 *MITF*-KO verses WT cells (FDR < 0.05) and genes directly inhibited by TFAP2,
922 based on RNA-seq, with TFAP2-inhibited enhancers, in *TFAP2*-KO verses WT cells
923 (FDR < 0.05). **(E)** Gene ontology (GO) biological process analysis (Top 5 hits) that
924 are enriched among MITF- and TFAP2-inhibited genes. GO analysis was performed
925 using PANTHER. **(F)** Dot plot of enrichment analysis showing the enrichment of
926 gene signatures from the literature in directly TFAP2-activated and TFAP2-inhibted
927 genes, based on RNA-seq, in *TFAP2*-KO and SK-MEL-28 cells. P value is red
928 lowest to blue highest; gene ratio is the ratio between genes and all genes in the GO
929 category. Analysis of directly TFAP2-activated genes associated with TFAP2-
930 dependent MITF peaks are shown (*).
931

932 **Figure S1: *tfap2e* mutant zebrafish do not display a melanocyte phenotype**
933 **whereas *tfap2a/e* double mutant zebrafish display a significant reduction in**
934 **melanocyte number**. **(A)** A 157 base pair mutation at the end of tfap2e exon 2
935 disrupts splicing and results in a premature stop codon. **(B)** PCR using primers in
936 tfap2e exon 2 and intron 2 (e2-i2) amplifies a band of the expected 450 base pair
937 size in tfap2e mutants but not wildtype (WT), whereas primers in exon 2 and exon 3
938 (e2-e3) amplify only in wildtype. NTC: not template control. **(C)** qRT-PCR analysis of
939 tfap2e expression shows that the transcript is strongly decreased in *tfap2e*-/-
940 mutants, consistent with nonsense-mediated decay (Student's t-test, **** $p<0.0001$).
941 **(D-E)** tfap2e mutant zebrafish at 36 hpf, *tfap2e*+/- **(D)** and *tfap2e*-/- **(E)** are
942 phenotypically indistinguishable. **(F)** Histogram illustrating the number of pigmented
943 melanocytes in the dorsum of *tfap2e*+/- and *tfap2e*-/- mutant zebrafish embryos,
944 **(G-H)** Zebrafish embryos from a *tfap2a*+/-;*tfap2e*+/- incross at 48 hpf. **(G)** A wildtype
945 embryo shows normal melanocyte patterning. **(H)** A tfap2a-/- mutant embryo has
946 fewer and paler embryonic melanocytes than wildtype**. (I)** tfap2a-/-;tfap2e+/- and (J)
947 tfap2a-/- ;tfap2e-/- appear phenotypically indistinguishable from tfap2a-/- at 48 hpf.
948
949 **Figure S2: TFAP2 binds to open and closed chromatin. (A)** Screenshot of IGV
950 genome browser (GRCH37/hg19), visualizing anti-TFAP2A and IgG CUT&RUN-seq
951 profiles. Peaks were called using MACS2 software (two independent replicates) and
952 are illustrated by blue bars under the anti-TFAP2A track. **(B)** Density heatmap
953 centred on the 36,867 TFAP2A peaks identified by anti-TFAP2A CUT&RUN in WT
954 SK-MEL-28 cells. Regions shown are +/- 3 kb from peak center, Peaks were
955 grouped by distance to an annotated transcriptional start site. Promoter peaks +/-
956 3kb from a TSS and enhancers >3 kb from an TSS. Anti-TFAP2A, anti-H3K4Me3
957 and anti-H3K27Ac CUT&RUN-seq, and ATAC-Seq profiles are shown. Normalized
958 reads (RPKM). **(C)** Histogram representing H3K27Ac signal, binned from low-high
959 read-depth on the x-axis and percentage of TFAP2A promoter peaks (black) and
960 TFAP2A enhancer peaks (red) on the y-axis. **(D)** Violin plots illustrating TFAP2A and
961 IgG normalized reads (RPKM) at nucleosome depleted regions (ATAC-peaks) and at
962 nucleosome occupied DNA (no ATAC-peak) **(E)** Density heatmap representing
963 TFAP2A CUT&RUN and ATAC-seq profiles at TFAP2A peaks that overlap
964 nucleosome depleted regions (ATAC-peaks) and at nucleosome bound DNA (no
965 ATAC-peak), the number of TFAP2A peaks in each group are as labeled.

966

967 **Figure S3: Example loci of TFAP2A peaks at open and closed chromatin. (A-B)**
968 IGV screenshots of TFAP2A peaks that **(A)** closed chromatin and **(B)** open
969 chromatin, based on ATAC-seq, in SK-MEL-28 cells. Genes names and distance to
970 a transcriptional start site as labeled. **(C)** HOMER motif analysis at TFAP2A peaks at
971 closed chromatin and **(D)** at open chromatin. TF, transcription factors; the top
972 ranking transcription factor motif is shown, with P-values calculated with HOMER-
973 based hypergeometric enrichment analysis.
974

975 **Figure S4: Generation of TFAP2A; TFAP2C double mutant SK-MEL-28 cell**
976 **lines. (A)** RNA-seq showing transcript counts of TFAP2 paralogs in SK-MEL-28
977 cells. Transcript counts for WT cells (n=4) and two *TFAP2A;TFAP2C* double
978 knockout clones (4 replicates each) are shown. The expression of WT and mutant
979 alleles of *TFAP2A* is comparable between cell lines whereas mutant alleles of
980 *TFAP2C* are strongly reduced. **(B)** Two guide RNAs (crRNAs) each were designed
981 to target exon 2 of *TFAP2A* and *TFAP2C* (yellow boxes). **(C)** A 401 base pair
982 inversion and a 452 base pair deletion at exon 2 of *TFAP2A* and *TFAP2C*,
983 respectively, was identified in clone 4.3. *TFAP2A* and *TFAP2C* mutant alleles
984 resulted in a frame-shift and premature stop codon in alleles of both genes. **(D)** A
985 405 base pair deletion at exon 2 of *TFAP2A* resulted in a frame-shift and premature
986 stop codon in clone 2.12. A 455 base pair deletion, and a 70 base pair insertion, 1
987 base pair deletion (Indel) was identified in exon 2 of *TFAP2C*. Such mutations
988 resulted in a frame-shift and premature stop codon. Additional permutations were not
989 identified at exon 2 of *TFAP2A* or *TFAP2C* in clone 4.3 or clone 2.12 cells. Inv;
990 inversion, Del; deletion. **(E)** Western blot analysis confirming loss of TFAP2A and
991 TFAP2C immunoactivity in clone 4.3 and clone 2.12 cell lines.
992

993 **Figure S5: TFAP2 paralogs activate and inhibit gene expression directly.**
994 **(A)** Volcano plot illustrating differential gene expression as determined by RNA
995 sequencing of *TFAP2*-KO cells (two independent clones (2.12 and 4.3); four
996 replicates each) versus WT cells (SK-MEL-28; four replicates). Log2 fold change
997 (FC) of mean transcript levels on the x-axis and log2 p-value on the y-axis. Red dots
998 represent direct target genes of TFAP2A that are differentially expressed (FDR <
999 0.05, log2FC > |1|), as determined by anti-TFAP2 CUT&RUN in SK-MEL-28 cells.

1000 Gray dots represent genes that are differentially expressed but not bound by TFAP2.
1001 The number and percentage of genes that are regulated by TFAP2 are specified.
1002 Directly TFAP2A-dependent genes were identified based on the gene-association
1003 rule (single nearest gene within 100 kb of a transcription start site).
1004
1005 **Figure S6: TFAP2 paralogs directly activate and inhibit promoters as pioneer**
1006 **factors. (A-D)** Screenshot of IGV genome browser (GRCH37/hg19), visualizing anti-
1007 TFAP2A CUT&RUN-seq (red), ATAC-seq (black), anti-H3K4Me3 CUT&RUN-seq
1008 (turquoise), anti-H3K27Ac CUT&RUN-seq (green) and RNA-seq (magenta) datasets
1009 at **(A-B)** TFAP2-activated promoters and **(C-D)** TFAP2-inhibited promoters.
1010 Genotypes as labeled; y-axes are grouped scaled per dataset. **(E-E'')** Violin plots
1011 representing **(E)** anti-H3K27Ac (two independent replicates) **(E')** ATAC-seq (four
1012 independent replicates) and **(E'')** anti-H3K4Me3 (two independent replicates)
1013 normalized reads at pioneered TFAP2-activated promoters. **(F-F'')** Violin plots
1014 representing **(F)** anti-H3K27Ac **(F')** ATAC-seq and **(E'')** anti-H3K4Me3 normalized
1015 reads at non-pioneered TFAP2-activated promoters. **(G-G'')** Violin plots representing
1016 **(G)** anti-H3K27Ac **(G')** ATAC-seq and **(G'')** anti-H3K4Me3 normalized reads at
1017 pioneered TFAP2-inhibited promoters. **(H-H'')** Violin plots representing **(H)** anti-
1018 H3K27Ac **(H')** ATAC-seq and **(H'')** anti-H3K4Me3 normalized reads at non-
1019 pioneered TFAP2-inhibited promoters. P-values shown were determined by Students
1020 t-test. **(I-L) H**ypergeometric analysis of TFAP2 regulated enhancers at TFAP2-
1021 activated (*) and TFAP2-inhibited (**) genes in *TFAP2*-KO cells (FDR < 0.05,
1022 |log2FC| > 1). The number of promoters in each category of TFAP2-regulated
1023 promoters is shown.
1024
1025 **Figure S7: Additional examples of TFAP2-activated and -inhibited promoters.**
1026 **(A-B)** Screenshots of IGV genome browser (GRCH37/hg19) visualizing anti-
1027 TFAP2A, anti-H3K4Me3, anti-H3K27Ac CUT&RUN-seq, ATAC-seq and RNA-seq
1028 profiles at **(A)** the TFAP2-activated *ZNF540* promoter and **(B)** the TFAP2-inhibited
1029 *S100A16* promoter. Genotypes as labeled; y-axes are grouped scaled per dataset.
1030
1031 **Figure S8: TFAP2 paralogs modulate the binding of MITF. (A)** Density heatmap
1032 centred on 9,413 peaks co-bound by TFAP2A and MITF, showing anti-TFAP2, anti-
1033 MITF, ATAC-seq, and anti-H3K27Ac CUT&RUN profiles in SK-MEL-28 cells.

1034 Regions shown are +/- 5 kb from peak center. **(B)** Violin plot showing anti-MITF
1035 CUT&RUN signal (RPKM) in *TFAP2*-KO and SK-MEL-28 cells at loci not bound by
1036 TFAP2A. ns; non-significant by Students t-test. **(C)** Scatterplot of TFAP2-dependent
1037 MITF peaks showing log2 normalized reads on the x-axis and log2FC on the y-axis
1038 in *TFAP2*-KO versus WT cells. **(D)** Screenshots of IGV genome browser
1039 (GRCH37/hg19); genotypes as labeled, visualizing anti-TFAP2A and anti-MITF
1040 CUT&RUN-seq and ATAC-seq profiles at TFAP2-dependent MITF peaks, mutually
1041 dependent MITF/TFAP2 peaks and an example of a non-overlapping, TFAP2-
1042 independent MITF peak. **(E)** Volcano plot showing increased H3K27Me3 CUT&RUN
1043 signal at mutually dependent TFAP2/MITF peaks in *MITF*-KO cells versus WT cells.
1044 P-values were determined by Students t-test. Normalized reads (RPKM), **(F-G)**
1045 Screenshots of IGV genome browser (GRCH37/hg19), visualizing anti-H3K27Me3
1046 CUT&RUN-seq profiles in *MIT*F-KO and WT cells. Peaks were called using MACS2
1047 software (two independent replicates) and are illustrated by blue bars. Two examples
1048 loci of mutually dependent TFAP2/MITF peaks showing increased H3K27Me3
1049 signals are shown, **(F)** at the *TRPM1* promoter and **(G)** at two *FRMD4B* enhancers.
1050 Mutually-dependent peaks are indicated by red arrows.
1051
1052 **Figure S9: Density heatmap of TFAP2 regulated MITF peaks.** Density heatmap
1053 centred on TFAP2 regulated MITF peaks (Top cluster) TFAP2-dependent MITF
1054 peaks, (Second cluster) Mutually dependent TFAP2/MITF peaks, (third cluster)
1055 TFAP2-inhibited MITF peaks and (forth cluster) independent peaks, showing two
1056 replicates of anti-MITF CUT&RUN in SK-MEL-28 and *TFAP2*-KO cells, and two
1057 replicates of anti-TFAP2A CUT&RUN in SK-MEL-28 and *MITF*-KO cells. Regions
1058 shown are +/- 5 kb from peak center.
1059
1060 **Figure S10: TFAP2 and MITF do not co-inhibit enhancers at TFAP2-inhibited or**
1061 **MITF-inhibited genes in SK-MEL-28 cells. (A-A')** Violin plot of TFAP2 dependent
1062 MITF peaks at TFAP2-inhibied enhancers (i.e. co-inhibited enhancers) showing **(B)**
1063 anti-MITF CUT&RUN and **(A')** ATAC-Seq profiles in *TFAP2*-KO and WT SK-MEL-28
1064 cells. Such loci were not significantly enriched at MITF-inhibited or TFAP2-inhibited
1065 genes. (A'') Schematic of TFAP2/ MITF co-inhibited enhancers. In this example
1066 TFAP2 is a pioneer factor recruiting MITF, in its repressor form, to condense
1067 chromatin. Loss of TFAP2 in TFAP2-KO cells results in loss of MITF-repressor

1068 binding and opening of chromatin by an alternative pioneer factor. **(B-B')** Violin plot
1069 of TFAP2-inhibited MITF peaks at modestly TFAP2-inhibted enhancers showing **(C)**
1070 anti-MITF CUT&RUN **(B')** ATAC-Seq profiles in *TFAP2*-KO and WT SK-MEL-28
1071 cells. Such loci were not significantly enriched at MITF-inhibited or TFAP2-inhibited
1072 genes. (B'') Schematic of TFAP2-inhibted MITF peaks at modestly inhibited
1073 enhancers (Log2FC > -0.5 – -1). In this example TFAP2 recruits a repressor protein
1074 and inhibits MITF binding in WT cells. In the absence of TFAP2, MITF recruits
1075 SWI/SNF and opens chromatin via an alternative pioneer factor.
1076
1077 **Figure S11: Genes that harbor TFAP2-independent anti-MITF peaks are**
1078 **enriched for cell cycle and DNA-repair. (A)** Plot-profile showing MITF CUT&RUN
1079 peak signal at TFAP2-independent MITF peaks in *TFAP2*-KO and WT SK-MEL-28
1080 cell lines. **(B)** Genes that harbor TFAP2-independent anti-MITF peaks were analyzed
1081 for enriched gene ontology biological process using GREAT (single nearest gene +/-
1082 100kb).
1083
1084 **Figure S12: Example of an TFAP2-dependent enhancer at intron 2 of MITF.**
1085 Screenshot of IGV genome browser (GRCH37/hg19) visualizing anti-TFAP2A,
1086 ATAC-seq, anti-H3K27Ac and RNA-seq profiles at intron 2 of MITF. Dashed
1087 rectangle indicates an TFAP2-dependent NDR. MITF and downstream regions are
1088 shown, blue arrows indicate strand orientation and horizontal rectangles the exons.
1089 Genotypes are as labeled; y-axes are grouped scaled per dataset.
1090
1091 **Figure S13: TFAP2 directly activates genes associated with cell differentiation**
1092 **and proliferation, and direct inhibits genes associated with cell adhesion and**
1093 **cell migration. (A-B)** The top 55 genes that are directly TFAP2-activated and
1094 associated with the GO terms **(A)** cell differentiation and pigmentation and **(B)**
1095 proliferation are represented by heatmap (log2FC). **(C)** the top 55 genes that are
1096 directly TFAP2-inhibited and associated with the GO terms cell adhesion and cell
1097 migration are represented by heatmap (log2FC). C1: *TFAP2*-KO clone 4.3, C2:
1098 *TFAP2*-KO clone 2.12. **(D)** Wound healing scratch-recovery-assay over 24 hours in
1099 WT and *TFAP2*-KO cells. *TFAP2*-KO cells show reduced migration capacity
1100 compared to wild type SK-MEL-28 cells.
1101

1102

1103 **References cited:**

1104

1105 Aras, S., Saladi, S.V., Basuroy, T., Marathe, H.G., Lores, P., de la Serna, I.L., 2019. BAF60A
1106 mediates interactions between the microphthalmia-associated transcription factor and the
1107 BRG1-containing SWI/SNF complex during melanocyte differentiation. J Cell Physiol 234,
1108 11780-11791.
1109 Atchison, M.L., 2014. Function of YY1 in Long-Distance DNA Interactions. Front Immunol
1110 5, 45.
1111 Bamforth, S.D., Braganca, J., Eloranta, J.J., Murdoch, J.N., Marques, F.I., Kranc, K.R.,
1112 Farza, H., Henderson, D.J., Hurst, H.C., Bhattacharya, S., 2001. Cardiac malformations,
1113 adrenal agenesis, neural crest defects and exencephaly in mice lacking Cited2, a new Tfap2
1114 co-activator. Nat Genet 29, 469-474.
1115 Barrallo-Gimeno, A., Holzschuh, J., Driever, W., Knapik, E.W., 2004. Neural crest survival
1116 and differentiation in zebrafish depends on mont blanc/tfap2a gene function. Development
1117 131, 1463-1477.
1118 Baxter, L.L., Loftus, S.K., Pavan, W.J., 2009. Networks and pathways in pigmentation,
1119 health, and disease. Wiley Interdiscip Rev Syst Biol Med 1, 359-371.
1120 Baxter, L.L., Watkins-Chow, D.E., Pavan, W.J., Loftus, S.K., 2019. A curated gene list for
1121 expanding the horizons of pigmentation biology. Pigment Cell Melanoma Res 32, 348-358.
1122 Bejjani, F., Evanno, E., Zibara, K., Piechaczyk, M., Jariel-Encontre, I., 2019. The AP-1
1123 transcriptional complex: Local switch or remote command? Biochim Biophys Acta Rev
1124 Cancer 1872, 11-23.
1125 Betancur, P., Bronner-Fraser, M., Sauka-Spengler, T., 2010. Assembling neural crest
1126 regulatory circuits into a gene regulatory network. Annu Rev Cell Dev Biol 26, 581-603.
1127 Braganca, J., Eloranta, J.J., Bamforth, S.D., Ibbitt, J.C., Hurst, H.C., Bhattacharya, S., 2003.
1128 Physical and functional interactions among AP-2 transcription factors, p300/CREB-binding
1129 protein, and CITED2. The Journal of biological chemistry 278, 16021-16029.
1130 Brewer, S., Jiang, X., Donaldson, S., Williams, T., Sucov, H.M., 2002. Requirement for AP-
1131 2alpha in cardiac outflow tract morphogenesis. Mech Dev 110, 139-149.
1132 Buenrostro, J.D., Giresi, P.G., Zaba, L.C., Chang, H.Y., Greenleaf, W.J., 2013. Transposition
1133 of native chromatin for fast and sensitive epigenomic profiling of open chromatin, DNA-
1134 binding proteins and nucleosome position. Nat Methods 10, 1213-1218.
1135 Buenrostro, J.D., Wu, B., Chang, H.Y., Greenleaf, W.J., 2015. ATAC-seq: A Method for
1136 Assaying Chromatin Accessibility Genome-Wide. Curr Protoc Mol Biol 109, 21.29.21-
1137 21.29.29.
1138 Campbell, N.R., Rao, A., Zhang, M., Baron, M., Heilmann, S., Deforet, M., Kenny, C.,
1139 Ferretti, L., Huang, T.-H., Garg, M., Nsengimana, J., Montal, E., Tagore, M., Hunter, M.,
1140 Newton-Bishop, J., Middleton, M.R., Corrie, P., Adams, D.J., Rabbie, R., Levesque, M.P.,
1141 Cornell, R.A., Yanai, I., Xavier, J.B., White, R.M., 2021. Cell state diversity promotes
1142 metastasis through heterotypic cluster formation in melanoma. Developmental Cell,
1143 2020.2008.2024.265140.
1144 Carreira, S., Goodall, J., Denat, L., Rodriguez, M., Nuciforo, P., Hoek, K.S., Testori, A.,
1145 Larue, L., Goding, C.R., 2006. Mitf regulation of Dia1 controls melanoma proliferation and
1146 invasiveness. Genes Dev 20, 3426-3439.
1147 Creyghton, M.P., Cheng, A.W., Welstead, G.G., Kooistra, T., Carey, B.W., Steine, E.J.,
1148 Hanna, J., Lodato, M.A., Frampton, G.M., Sharp, P.A., Boyer, L.A., Young, R.A., Jaenisch,

1149 R., 2010. Histone H3K27ac separates active from poised enhancers and predicts
1150 developmental state. Proc Natl Acad Sci U S A 107, 21931-21936.
1151 de la Serna, I.L., Ohkawa, Y., Higashi, C., Dutta, C., Osias, J., Kommajosyula, N.,
1152 Tachibana, T., Imbalzano, A.N., 2006. The microphthalmia-associated transcription factor
1153 requires SWI/SNF enzymes to activate melanocyte-specific genes. J Biol Chem 281, 20233-
1154 20241.
1155 Dilshat, R., Fock, V., Kenny, C., Gerritsen, I., Lasseur, R.M.J., Travnickova, J., Eichhoff,
1156 O.M., Cerny, P., Moller, K., Sigurbjornsdottir, S., Kirty, K., Einarsdottir, B.O., Cheng, P.F.,
1157 Levesque, M., Cornell, R.A., Patton, E.E., Larue, L., de Tayrac, M., Magnusdottir, E., Helga
1158 Ogmundsdottir, M., Steingrimsson, E., 2021. MITF reprograms the extracellular matrix and
1159 focal adhesion in melanoma. Elife 10.
1160 Dobin, A., Davis, C.A., Schlesinger, F., Drenkow, J., Zaleski, C., Jha, S., Batut, P., Chaisson,
1161 M., Gingeras, T.R., 2013. STAR: ultrafast universal RNA-seq aligner. Bioinformatics 29, 15-
1162 21.
1163 Du, J., Li, L., Ou, Z., Kong, C., Zhang, Y., Dong, Z., Zhu, S., Jiang, H., Shao, Z., Huang, B.,
1164 Lu, J., 2012. FOXC1, a target of polycomb, inhibits metastasis of breast cancer cells. Breast
1165 Cancer Res Treat 131, 65-73.
1166 Eckert, D., Buhl, S., Weber, S., Jager, R., Schorle, H., 2005. The AP-2 family of transcription
1167 factors. Genome Biol 6, 246.
1168 Fernandez Garcia, M., Moore, C.D., Schulz, K.N., Alberto, O., Donague, G., Harrison, M.M.,
1169 Zhu, H., Zaret, K.S., 2019. Structural Features of Transcription Factors Associating with
1170 Nucleosome Binding. Mol Cell 75, 921-932 e926.
1171 Goding, C.R., 2000. Mitf from neural crest to melanoma: signal transduction and
1172 transcription in the melanocyte lineage. Genes Dev 14, 1712-1728.
1173 Grossman, S.R., Engreitz, J., Ray, J.P., Nguyen, T.H., Hacohen, N., Lander, E.S., 2018.
1174 Positional specificity of different transcription factor classes within enhancers. Proc Natl
1175 Acad Sci U S A 115, E7222-E7230.
1176 Hartman, M.L., Czyz, M., 2015. MITF in melanoma: mechanisms behind its expression and
1177 activity. Cell Mol Life Sci 72, 1249-1260.
1178 Higdon, C.W., Mitra, R.D., Johnson, S.L., 2013. Gene expression analysis of zebrafish
1179 melanocytes, iridophores, and retinal pigmented epithelium reveals indicators of biological
1180 function and developmental origin. PLoS One 8, e67801.
1181 Hoek, K.S., Eichhoff, O.M., Schlegel, N.C., Döbbeling, U., Kobert, N., Schaerer, L., Hemmi,
1182 S., Dummer, R., 2008a. In vivo switching of human melanoma cells between proliferative
1183 and invasive states. Cancer Res 68, 650-656.
1184 Hoek, K.S., Schlegel, N.C., Brafford, P., Sucker, A., Ugurel, S., Kumar, R., Weber, B.L.,
1185 Nathanson, K.L., Phillips, D.J., Herlyn, M., Schadendorf, D., Dummer, R., 2006. Metastatic
1186 potential of melanomas defined by specific gene expression profiles with no BRAF signature.
1187 Pigment Cell Res 19, 290-302.
1188 Hoek, K.S., Schlegel, N.C., Eichhoff, O.M., Widmer, D.S., Praetorius, C., Einarsson, S.O.,
1189 Valgeirsdottir, S., Bergsteinsdottir, K., Schepsky, A., Dummer, R., Steingrimsson, E., 2008b.
1190 Novel MITF targets identified using a two-step DNA microarray strategy. Pigment Cell
1191 Melanoma Res 21, 665-676.
1192 Huang, S., Jean, D., Luca, M., Tainsky, M.A., Bar-Eli, M., 1998. Loss of AP-2 results in
1193 downregulation of c-KIT and enhancement of melanoma tumorigenicity and metastasis.
1194 EMBO J 17, 4358-4369.
1195 Jonsson, G., Busch, C., Knappskog, S., Geisler, J., Miletic, H., Ringner, M., Lillehaug, J.R.,
1196 Borg, A., Lonning, P.E., 2010. Gene expression profiling-based identification of molecular
1197 subtypes in stage IV melanomas with different clinical outcome. Clin Cancer Res 16, 3356-
1198 3367.

1199 Keenen, B., Qi, H., Saladi, S.V., Yeung, M., de la Serna, I.L., 2010. Heterogeneous
1200 SWI/SNF chromatin remodeling complexes promote expression of microphthalmia-
1201 associated transcription factor target genes in melanoma. Oncogene 29, 81-92.
1202 Kim, S., Yu, N.K., Kaang, B.K., 2015. CTCF as a multifunctional protein in genome
1203 regulation and gene expression. Exp Mol Med 47, e166.
1204 Knight, R.D., Javidan, Y., Nelson, S., Zhang, T., Schilling, T., 2004. Skeletal and pigment
1205 cell defects in the lockjaw mutant reveal multiple roles for zebrafish tfap2a in neural crest
1206 development. Dev Dyn 229, 87-98.
1207 Knight, R.D., Nair, S., Nelson, S.S., Afshar, A., Javidan, Y., Geisler, R., Rauch, G.J.,
1208 Schilling, T.F., 2003. lockjaw encodes a zebrafish tfap2a required for early neural crest
1209 development. Development 130, 5755-5768.
1210 Kołat, D., Kałuzińska, Ż., Bednarek, A.K., Płuciennik, E., 2021. WWOX Loses the Ability to
1211 Regulate Oncogenic AP-2γ and Synergizes with Tumor Suppressor AP-2α in High-Grade
1212 Bladder Cancer. Cancers (Basel) 13.
1213 Kuckenberg, P., Kubaczka, C., Schorle, H., 2012. The role of transcription factor
1214 Tcfap2c/TFAP2C in trophectoderm development. Reprod Biomed Online 25, 12-20.
1215 Lang, D., Lu, M.M., Huang, L., Engleka, K.A., Zhang, M., Chu, E.Y., Lipner, S., Skoultchi,
1216 A., Millar, S.E., Epstein, J.A., 2005. Pax3 functions at a nodal point in melanocyte stem cell
1217 differentiation. Nature 433, 884-887.
1218 Langmead, B., Salzberg, S.L., 2012. Fast gapped-read alignment with Bowtie 2. Nat Methods
1219 9, 357-359.
1220 Langmead, B., Trapnell, C., Pop, M., Salzberg, S.L., 2009. Ultrafast and memory-efficient
1221 alignment of short DNA sequences to the human genome. Genome Biol 10, R25.
1222 Laurette, P., Strub, T., Koludrovic, D., Keime, C., Le Gras, S., Seberg, H., Van Otterloo, E.,
1223 Imrichova, H., Siddaway, R., Aerts, S., Cornell, R.A., Mengus, G., Davidson, I., 2015.
1224 Transcription factor MITF and remodeller BRG1 define chromatin organisation at regulatory
1225 elements in melanoma cells. Elife 4.
1226 Lee, B.K., Uprety, N., Jang, Y.J., Tucker, S.K., Rhee, C., LeBlanc, L., Beck, S., Kim, J.,
1227 2018. Fosl1 overexpression directly activates trophoblast-specific gene expression programs
1228 in embryonic stem cells. Stem Cell Res 26, 95-102.
1229 Leroy, B., Girard, L., Hollestelle, A., Minna, J.D., Gazdar, A.F., Soussi, T., 2014. Analysis of
1230 TP53 mutation status in human cancer cell lines: a reassessment. Hum Mutat 35, 756-765.
1231 Li, L., Wang, Y., Torkelson, J.L., Shankar, G., Pattison, J.M., Zhen, H.H., Fang, F., Duren,
1232 Z., Xin, J., Gaddam, S., Melo, S.P., Piekos, S.N., Li, J., Liaw, E.J., Chen, L., Li, R., Wernig,
1233 M., Wong, W.H., Chang, H.Y., Oro, A.E., 2019. TFAP2C- and p63-Dependent Networks
1234 Sequentially Rearrange Chromatin Landscapes to Drive Human Epidermal Lineage
1235 Commitment. Cell Stem Cell 24, 271-284 e278.
1236 Li, W., Cornell, R.A., 2007. Redundant activities of Tfap2a and Tfap2c are required for
1237 neural crest induction and development of other non-neural ectoderm derivatives in zebrafish
1238 embryos. Dev Biol 304, 338-354.
1239 Lin, C.Y., Chao, A., Wang, T.H., Lee, L.Y., Yang, L.Y., Tsai, C.L., Wang, H.S., Lai, C.H.,
1240 2016. Nucleophosmin/B23 is a negative regulator of estrogen receptor alpha expression via
1241 AP2gamma in endometrial cancer cells. Oncotarget 7, 60038-60052.
1242 Liu, H., Duncan, K., Helverson, A., Kumari, P., Mumm, C., Xiao, Y., Carlson, J.C.,
1243 Darbellay, F., Visel, A., Leslie, E., Breheny, P., Erives, A.J., Cornell, R.A., 2020. Analysis of
1244 zebrafish periderm enhancers facilitates identification of a regulatory variant near human
1245 KRT8/18. Elife 9.
1246 Liu, H., Tan, B.C., Tseng, K.H., Chuang, C.P., Yeh, C.W., Chen, K.D., Lee, S.C., Yung,
1247 B.Y., 2007. Nucleophosmin acts as a novel AP2alpha-binding transcriptional corepressor
1248 during cell differentiation. EMBO Rep 8, 394-400.

1249 Love, M.I., Huber, W., Anders, S., 2014. Moderated estimation of fold change and dispersion
1250 for RNA-seq data with DESeq2. Genome Biol 15, 550.
1251 Luo, T., Matsuo-Takasaki, M., Thomas, M.L., Weeks, D.L., Sargent, T.D., 2002.
1252 Transcription factor AP-2 is an essential and direct regulator of epidermal development in
1253 Xenopus. Dev Biol 245, 136-144.
1254 Mavrothalassitis, G., Ghysdael, J., 2000. Proteins of the ETS family with transcriptional
1255 repressor activity. Oncogene 19, 6524-6532.
1256 Mayran, A., Khetchoumian, K., Hariri, F., Pastinen, T., Gauthier, Y., Balsalobre, A., Drouin,
1257 J., 2018. Pioneer factor Pax7 deploys a stable enhancer repertoire for specification of cell
1258 fate. Nat Genet 50, 259-269.
1259 McLean, C.Y., Bristor, D., Hiller, M., Clarke, S.L., Schaar, B.T., Lowe, C.B., Wenger, A.M.,
1260 Bejerano, G., 2010. GREAT improves functional interpretation of cis-regulatory regions. Nat
1261 Biotechnol 28, 495-501.
1262 Meers, M.P., Bryson, T.D., Henikoff, J.G., Henikoff, S., 2019. Improved CUT&RUN
1263 chromatin profiling tools. Elife 8.
1264 Mi, H., Ebert, D., Muruganujan, A., Mills, C., Albou, L.P., Mushayamaha, T., Thomas, P.D.,
1265 2021. PANTHER version 16: a revised family classification, tree-based classification tool,
1266 enhancer regions and extensive API. Nucleic Acids Res 49, D394-d403.
1267 Miller, J.C., Holmes, M.C., Wang, J., Guschin, D.Y., Lee, Y.L., Rupniewski, I., Beausejour,
1268 C.M., Waite, A.J., Wang, N.S., Kim, K.A., Gregory, P.D., Pabo, C.O., Rebar, E.J., 2007. An
1269 improved zinc-finger nuclease architecture for highly specific genome editing. Nat
1270 Biotechnol 25, 778-785.
1271 Mitchell, P.J., Timmons, P.M., Hebert, J.M., Rigby, P.W., Tjian, R., 1991. Transcription
1272 factor AP-2 is expressed in neural crest cell lineages during mouse embryogenesis. Genes
1273 Dev 5, 105-119.
1274 Mollaaghababa, R., Pavan, W.J., 2003. The importance of having your SOX on: role of
1275 SOX10 in the development of neural crest-derived melanocytes and glia. Oncogene 22, 3024-
1276 3034.
1277 Moser, M., Ruschoff, J., Buettner, R., 1997. Comparative analysis of AP-2 alpha and AP-2
1278 beta gene expression during murine embryogenesis. Developmental Dynamics 208, 115-124.
1279 Pastor, W.A., Liu, W., Chen, D., Ho, J., Kim, R., Hunt, T.J., Lukianchikov, A., Liu, X., Polo,
1280 J.M., Jacobsen, S.E., Clark, A.T., 2018. TFAP2C regulates transcription in human naive
1281 pluripotency by opening enhancers. Nat Cell Biol 20, 553-564.
1282 Pekowska, A., Benoukraf, T., Zacarias-Cabeza, J., Belhocine, M., Koch, F., Holota, H.,
1283 Imbert, J., Andrau, J.C., Ferrier, P., Spicuglia, S., 2011. H3K4 tri-methylation provides an
1284 epigenetic signature of active enhancers. EMBO J 30, 4198-4210.
1285 Petruk, S., Cai, J., Sussman, R., Sun, G., Kovermann, S.K., Mariani, S.A., Calabretta, B.,
1286 McMahon, S.B., Brock, H.W., Iacovitti, L., Mazo, A., 2017. Delayed Accumulation of
1287 H3K27me3 on Nascent DNA Is Essential for Recruitment of Transcription Factors at Early
1288 Stages of Stem Cell Differentiation. Mol Cell 66, 247-257 e245.
1289 Pihlajamaa, P., Sahu, B., Lyly, L., Aittomaki, V., Hautaniemi, S., Janne, O.A., 2014. Tissue-
1290 specific pioneer factors associate with androgen receptor cistromes and transcription
1291 programs. EMBO J 33, 312-326.
1292 Praetorius, C., Grill, C., Stacey, S.N., Metcalf, A.M., Gorkin, D.U., Robinson, K.C., Van
1293 Otterloo, E., Kim, R.S., Bergsteinsdottir, K., Ogmundsdottir, M.H., Magnusdottir, E., Mishra,
1294 P.J., Davis, S.R., Guo, T., Zaidi, M.R., Helgason, A.S., Sigurdsson, M.I., Meltzer, P.S.,
1295 Merlino, G., Petit, V., Larue, L., Loftus, S.K., Adams, D.R., Sobhiafshar, U., Emre, N.C.,
1296 Pavan, W.J., Cornell, R., Smith, A.G., McCallion, A.S., Fisher, D.E., Stefansson, K., Sturm,
1297 R.A., Steingrimsson, E., 2013. A polymorphism in IRF4 affects human pigmentation through
1298 a tyrosinase-dependent MITF/TFAP2A pathway. Cell 155, 1022-1033.

1299 Rambow, F., Job, B., Petit, V., Gesbert, F., Delmas, V., Seberg, H., Meurice, G., Van
1300 Otterloo, E., Dessen, P., Robert, C., Gautheret, D., Cornell, R.A., Sarasin, A., Larue, L.,
1301 2015. New Functional Signatures for Understanding Melanoma Biology from Tumor Cell
1302 Lineage-Specific Analysis. Cell Rep 13, 840-853.
1303 Rambow, F., Marine, J.C., Goding, C.R., 2019. Melanoma plasticity and phenotypic
1304 diversity: therapeutic barriers and opportunities. Genes Dev 33, 1295-1318.
1305 Rambow, F., Rogiers, A., Marin-Bejar, O., Aibar, S., Femel, J., Dewaele, M., Karras, P.,
1306 Brown, D., Chang, Y.H., Debiec-Rychter, M., Adriaens, C., Radaelli, E., Wolter, P., Bechter,
1307 O., Dummer, R., Levesque, M., Piris, A., Frederick, D.T., Boland, G., Flaherty, K.T., van den
1308 Oord, J., Voet, T., Aerts, S., Lund, A.W., Marine, J.C., 2018. Toward Minimal Residual
1309 Disease-Directed Therapy in Melanoma. Cell 174, 843-855 e819.
1310 Ramírez, F., Ryan, D.P., Grüning, B., Bhardwaj, V., Kilpert, F., Richter, A.S., Heyne, S.,
1311 Dündar, F., Manke, T., 2016. deepTools2: a next generation web server for deep-sequencing
1312 data analysis. Nucleic Acids Res 44, W160-165.
1313 Ringrose, L., Paro, R., 2004. Epigenetic regulation of cellular memory by the Polycomb and
1314 Trithorax group proteins. Annu Rev Genet 38, 413-443.
1315 Ross-Innes, C.S., Stark, R., Teschendorff, A.E., Holmes, K.A., Ali, H.R., Dunning, M.J.,
1316 Brown, G.D., Gojis, O., Ellis, I.O., Green, A.R., Ali, S., Chin, S.F., Palmieri, C., Caldas, C.,
1317 Carroll, J.S., 2012. Differential oestrogen receptor binding is associated with clinical
1318 outcome in breast cancer. Nature 481, 389-393.
1319 Sander, J.D., Dahlborg, E.J., Goodwin, M.J., Cade, L., Zhang, F., Cifuentes, D., Curtin, S.J.,
1320 Blackburn, J.S., Thibodeau-Beganny, S., Qi, Y., Pierick, C.J., Hoffman, E., Maeder, M.L.,
1321 Khayter, C., Reyon, D., Dobbs, D., Langenau, D.M., Stupar, R.M., Giraldez, A.J., Voytas,
1322 D.F., Peterson, R.T., Yeh, J.R., Joung, J.K., 2011. Selection-free zinc-finger-nuclease
1323 engineering by context-dependent assembly (CoDA). Nat Methods 8, 67-69.
1324 Sander, J.D., Maeder, M.L., Reyon, D., Voytas, D.F., Joung, J.K., Dobbs, D., 2010. ZiFiT
1325 (Zinc Finger Targeter): an updated zinc finger engineering tool. Nucleic Acids Res 38,
1326 W462-468.
1327 Schorle, H., Meier, P., Buchert, M., Jaenisch, R., Mitchell, P.J., 1996. Transcription factor
1328 AP-2 essential for cranial closure and craniofacial development. Nature 381, 235-238.
1329 Seberg, H.E., Van Otterloo, E., Cornell, R.A., 2017a. Beyond MITF: Multiple transcription
1330 factors directly regulate the cellular phenotype in melanocytes and melanoma. Pigment Cell
1331 Melanoma Res 30, 454-466.
1332 Seberg, H.E., Van Otterloo, E., Loftus, S.K., Liu, H., Bonde, G., Sompallae, R., Gildea, D.E.,
1333 Santana, J.F., Manak, J.R., Pavan, W.J., Williams, T., Cornell, R.A., 2017b. TFAP2 paralogs
1334 regulate melanocyte differentiation in parallel with MITF. PLoS Genet 13, e1006636.
1335 Sekiya, T., Zaret, K.S., 2007. Repression by Groucho/TLE/Grg proteins: genomic site
1336 recruitment generates compacted chromatin in vitro and impairs activator binding in vivo.
1337 Mol Cell 28, 291-303.
1338 Sherwood, R.I., Hashimoto, T., O'Donnell, C.W., Lewis, S., Barkal, A.A., van Hoff, J.P.,
1339 Karun, V., Jaakkola, T., Gifford, D.K., 2014. Discovery of directional and nondirectional
1340 pioneer transcription factors by modeling DNase profile magnitude and shape. Nat
1341 Biotechnol 32, 171-178.
1342 Skene, P.J., Henikoff, S., 2017. An efficient targeted nuclease strategy for high-resolution
1343 mapping of DNA binding sites. Elife 6.
1344 Strub, T., Giuliano, S., Ye, T., Bonet, C., Keime, C., Kobi, D., Le Gras, S., Cormont, M.,
1345 Ballotti, R., Bertolotto, C., Davidson, I., 2011. Essential role of microphthalmia transcription
1346 factor for DNA replication, mitosis and genomic stability in melanoma. Oncogene 30, 2319-
1347 2332.

1348 Swinstead, E.E., Miranda, T.B., Paakinaho, V., Baek, S., Goldstein, I., Hawkins, M.,
1349 Karpova, T.S., Ball, D., Mazza, D., Lavis, L.D., Grimm, J.B., Morisaki, T., Grontved, L.,
1350 Presman, D.M., Hager, G.L., 2016a. Steroid Receptors Reprogram FoxA1 Occupancy
1351 through Dynamic Chromatin Transitions. Cell 165, 593-605.
1352 Swinstead, E.E., Paakinaho, V., Presman, D.M., Hager, G.L., 2016b. Pioneer factors and
1353 ATP-dependent chromatin remodeling factors interact dynamically: A new perspective:
1354 Multiple transcription factors can effect chromatin pioneer functions through dynamic
1355 interactions with ATP-dependent chromatin remodeling factors. Bioessays 38, 1150-1157.
1356 Tan, C.C., Sindhu, K.V., Li, S., Nishio, H., Stoller, J.Z., Oishi, K., Puttreddy, S., Lee, T.J.,
1357 Epstein, J.A., Walsh, M.J., Gelb, B.D., 2008. Transcription factor Ap2delta associates with
1358 Ash2l and ALR, a trithorax family histone methyltransferase, to activate Hoxc8 transcription.
1359 Proc Natl Acad Sci U S A 105, 7472-7477.
1360 Tan, S.K., Lin, Z.H., Chang, C.W., Varang, V., Chng, K.R., Pan, Y.F., Yong, E.L., Sung,
1361 W.K., Cheung, E., 2011. AP-2gamma regulates oestrogen receptor-mediated long-range
1362 chromatin interaction and gene transcription. EMBO J 30, 2569-2581.
1363 Tirosh, I., Izar, B., Prakadan, S.M., Wadsworth, M.H., 2nd, Treacy, D., Trombetta, J.J.,
1364 Rotem, A., Rodman, C., Lian, C., Murphy, G., Fallahi-Sichani, M., Dutton-Regester, K., Lin,
1365 J.R., Cohen, O., Shah, P., Lu, D., Genshaft, A.S., Hughes, T.K., Ziegler, C.G., Kazer, S.W.,
1366 Gaillard, A., Kolb, K.E., Villani, A.C., Johannessen, C.M., Andreev, A.Y., Van Allen, E.M.,
1367 Bertagnolli, M., Sorger, P.K., Sullivan, R.J., Flaherty, K.T., Frederick, D.T., Jane-Valbuena,
1368 J., Yoon, C.H., Rozenblatt-Rosen, O., Shalek, A.K., Regev, A., Garraway, L.A., 2016.
1369 Dissecting the multicellular ecosystem of metastatic melanoma by single-cell RNA-seq.
1370 Science 352, 189-196.
1371 Tsoi, J., Robert, L., Paraiso, K., Galvan, C., Sheu, K.M., Lay, J., Wong, D.J.L., Atefi, M.,
1372 Shirazi, R., Wang, X., Braas, D., Grasso, C.S., Palaskas, N., Ribas, A., Graeber, T.G., 2018.
1373 Multi-stage Differentiation Defines Melanoma Subtypes with Differential Vulnerability to
1374 Drug-Induced Iron-Dependent Oxidative Stress. Cancer Cell 33, 890-904 e895.
1375 Van Otterloo, E., Li, W., Bonde, G., Day, K.M., Hsu, M.Y., Cornell, R.A., 2010.
1376 Differentiation of zebrafish melanophores depends on transcription factors AP2 alpha and
1377 AP2 epsilon. PLoS Genet 6.
1378 Van Otterloo, E., Li, W., Garnett, A., Cattell, M., Medeiros, D.M., Cornell, R.A., 2012.
1379 Novel Tfap2-mediated control of soxE expression facilitated the evolutionary emergence of
1380 the neural crest. Development 139, 720-730.
1381 Verfaillie, A., Imrichova, H., Atak, Z.K., Dewaele, M., Rambow, F., Hulselmans, G.,
1382 Christiaens, V., Svetlichnyy, D., Luciani, F., Van den Mooter, L., Claerhout, S., Fiers, M.,
1383 Journe, F., Ghanem, G.E., Herrmann, C., Halder, G., Marine, J.C., Aerts, S., 2015. Decoding
1384 the regulatory landscape of melanoma reveals TEADS as regulators of the invasive cell state.
1385 Nat Commun 6, 6683.
1386 Vierbuchen, T., Ling, E., Cowley, C.J., Couch, C.H., Wang, X., Harmin, D.A., Roberts,
1387 C.W.M., Greenberg, M.E., 2017. AP-1 Transcription Factors and the BAF Complex Mediate
1388 Signal-Dependent Enhancer Selection. Mol Cell 68, 1067-1082.e1012.
1389 Voss, T.C., Hager, G.L., 2014. Dynamic regulation of transcriptional states by chromatin and
1390 transcription factors. Nat Rev Genet 15, 69-81.
1391 Wang, X., Bolotin, D., Chu, D.H., Polak, L., Williams, T., Fuchs, E., 2006. AP-2alpha: a
1392 regulator of EGF receptor signaling and proliferation in skin epidermis. J Cell Biol 172, 409-
1393 421.
1394 Wang, X., Pasolli, H.A., Williams, T., Fuchs, E., 2008. AP-2 factors act in concert with
1395 Notch to orchestrate terminal differentiation in skin epidermis. J Cell Biol 183, 37-48.
1396 Watts, J.A., Zhang, C., Klein-Szanto, A.J., Kormish, J.D., Fu, J., Zhang, M.Q., Zaret, K.S.,
1397 2011. Study of FoxA pioneer factor at silent genes reveals Rfx-repressed enhancer at Cdx2

1398 and a potential indicator of esophageal adenocarcinoma development. PLoS Genet 7,
1399 e1002277.
1400 White, J.R., Thompson, D.T., Koch, K.E., Kiriazov, B.S., Beck, A.C., van der Heide, D.M.,
1401 Grimm, B.G., Kulak, M.V., Weigel, R.J., 2021. AP-2alpha-mediated activation of E2F and
1402 EZH2 drives melanoma metastasis. Cancer Res.
1403 Wilson, B.G., Wang, X., Shen, X., McKenna, E.S., Lemieux, M.E., Cho, Y.J., Koellhoffer,
1404 E.C., Pomeroy, S.L., Orkin, S.H., Roberts, C.W., 2010. Epigenetic antagonism between
1405 polycomb and SWI/SNF complexes during oncogenic transformation. Cancer Cell 18, 316-
1406 328.
1407 Wong, P.P., Miranda, F., Chan, K.V., Berlato, C., Hurst, H.C., Scibetta, A.G., 2012. Histone
1408 demethylase KDM5B collaborates with TFAP2C and Myc to repress the cell cycle inhibitor
1409 p21(cip) (CDKN1A). Mol Cell Biol 32, 1633-1644.
1410 Yu, G., Wang, L.G., Han, Y., He, Q.Y., 2012. clusterProfiler: an R package for comparing
1411 biological themes among gene clusters. Omics 16, 284-287.
1412 Zaret, K.S., 2020. Pioneer Transcription Factors Initiating Gene Network Changes. Annu Rev
1413 Genet 54, 367-385.
1414 Zaret, K.S., Carroll, J.S., 2011. Pioneer transcription factors: establishing competence for
1415 gene expression. Genes Dev 25, 2227-2241.
1416 Zhang, Y., Liu, T., Meyer, C.A., Eeckhoute, J., Johnson, D.S., Bernstein, B.E., Nusbaum, C.,
1417 Myers, R.M., Brown, M., Li, W., Liu, X.S., 2008. Model-based analysis of ChIP-Seq
1418 (MACS). Genome Biol 9, R137.
1419